NEUTRON STRAIN TOMOGRAPHY

A dissertation submitted in partial fulfillment of the requirements for the degree of Master of Research at the University of Oxford

Brian Abbey

Worcester College



Supervised by
Professor Alexander M. Korsunsky
Submitted: October, 2012

School of Engineering Science
University of Oxford
October 2012

Declaration

The work presented in this these is the original work of the author and contains no material which is the result of collaboration except where otherwise stated.

This dissertation is not the same as any other submitted by the author for a degree or diploma or any other qualification at any other university. No part of this work has already been or is being concurrently submitted for any such degree, diploma or other qualification.

This dissertation does not exceed 60,000 words in length.

Brian Abbey
October 2012

SUMMARY

This thesis concerns the development of a technique known as 'neutron strain tomography', in order to non-destructively map, in three dimensions, residual elastic strain. The fundamental idea behind this research is that the strain values provided by through-thickness transmission strain measurements are the result of averaging a number of strains within the sample. If a two-dimensional energy-resolving pixellated detector is used to record the transmission strains, a spatially resolved two-dimensional image of the average strain within the sample is obtained. This implies that if one records two-dimensional average strain data from the same sample from a number of different orientations there may be a route to reconstructing a set of higher dimensional volume data based on these two-dimensional datasets.

The principle aim on this thesis has been to help develop neutron strain tomography into a viable tool for three-dimensional strain imaging. The main themes explored in this research are the generalisation of the method to arbitrary strain fields and its extension to high resolution strain 'imaging'.

Solutions and challenges associated with the first theme are outlined in chapters 2 and 3 which lay the theoretical foundations for the algorithms we employ in this research and the results obtained using these algorithms respectively. The second theme, resolution, is discussed in chapter 4 where the possibilities offered by high-resolution, energy resolving, neutron detectors is discussed in the context of neutron strain tomography. The descriptions of the algorithms, the comparison of possible approaches, and the improvements afforded by new detector technologies is intended to serve as an entry point guide for researchers wishing to further continue this work.

ACKNOWLEDGEMENTS

During the course of this research project many people have given me advice and support which proved invaluable. The following people are those to whom I would like to extend special thanks.

Principally I would like to thank my supervisor Prof. Alexander Korsunsky whose patience, experience and dedication to the project helped to make my time at Oxford a rewarding one. In particular, thank you for the continual support and sage advice, this was very much appreciated!

Secondly, I would like to thank the other members of our group in Oxford, Dr Felix Hofmann, Dr Xu Song, Dr Johnathan Belnoue, Nikos Baimpas to name but a few. They have provided immense support over years. I wish them all the best of luck for the future.

I would also like to thank Dr Shu Yan Zhang of the ISIS neutron facility, who has guided all aspects of the experimental portion of the project and has given much advice on the interpretation of data.

Thanks go as well to the mechanical workshop staff, in particular Mr Richard Duffin, for their correction and construction of my designs and also willingness to help no matter how short the notice.

I would also sincerely like to thank Dr Igor Dolbnya of the Diamond Light Source, his commitment to the microdiffraction measurements has been superb, and it without doubt one of the reasons the project continues to develop.

The other staff at the DLS (too numerous to list here) who have worked tirelessly to help get our experiments up and running are also acknowledged.

Finally, thanks also go to the EPSRC and Rolls Royce for financial support.

TABLE of CONTENTS

INTRODUCTION and FUNDAMENTAL PRINCIPLES

1.1 INTRODUCTION 1

1.2 NEUTRON DIFFRACTION 1

1.2.1 Fundamental Principles of Neutron Diffraction 1

1.2.2 Diffraction from Crystalline Solids 4

1.2.3 Angle-Dispersive Neutron Diffraction Strain Measurement 7

1.2.4 Measuring a strain-free reference 12

1.2.5 Stresses at multiple length scale 12

1.2.6 Future of angle-resolved neutron diffraction 13

1.3 Time-of-Flight Neutron Techniques 13

1.3.1 Time-of-Flight Measurements 13

1.3.2 Energy-dispersive neutron diffraction strain measurements 14

1.3.3 Bragg-edge Neutron Transmission Measurements 18

1.3.4 Strain Imaging using Bragg Edge Transmission 18

1.4 REFERENCES 21

THE DEVELOPMENT of NEUTRON STRAIN TOMOGRAPHY

2.1 INTRODUCTION 22

2.1 MOTIVATION for NEUTRON STRAIN TOMOGRAPHY 22

2.3 Fundamental Principles 24

2.4 Strain Tomography 28

2.4.1 Introduction 28

2.4.2 Previous Approaches to Strain Tomography 29

2.4.3 Multi-Component Strain Tomography 35

2.4.4 Linear Tent Function Representation 35

2.4.5 Parameterised model approach 39

2.4.6 Combined Neutron Diffraction and Strain Tomography 41
2.7 REFERENCES 42

EXPERIMENTAL RESULTS

3.1 INTRODUCTION 44
3.2 SAMPLE PREPERATION and MEASUREMENT 44
3.2.1 Literature Review: VAMAS and Quenched Cylinder Samples 44
3.3 RESULTS for RING and PLUG SAMPLE 47
3.3.1 Ring-and-Plug: Linear Tent Function Representation 47
3.4 RESULTS for QUENCHED CYLINDER 52
3.4.1 Quenched cylinder: Model Constraint 52
3.4.2 Quenched cylinder: Combined Diffraction and Strain Tomography 54
3.5 RESULTS for STEEL BENT BEAM 55
3.5.1 Steel Bent Beam: Comparison with Finite Element Modelling 55
3.6 SUMMARY of APPROACHES 60
3.7 REFERENCES 61

CONCLUSIONS AND SUGGESTIONS FOR FUTURE WORK

4.1 INTRODUCTION 62

4.2 Approaches to Neutron Strain Tomography 62

4.3 Future Work 64

4.3.1 Literature Review: High Resolution Neutron Strain Imaging 64

4.3.2 Latest results: strain tomography using TIMEPIX 70

4.3.3 Future research: planned experiments and ideas for further work 72

4.4 References 72

Appendix Publications Arising From This Work 74

INTRODUCTION and FUNDAMENTAL PRINCIPLES

CHAPTER 1

1.1 INTRODUCTION

In this introductory chapter the fundamental ideas behind neutron diffraction, the primary technique used to carry out the work described in this thesis, are given. The discussion then focuses on the main topic of this thesis, namely: how strain can be extracted from two-dimensional transmission neutron measurements. The final part of this chapter examines some recent work in the area of Bragg edge neutron transmission and provides a useful segue into the topic of neutron strain tomography.

1.2 NEUTRON DIFFRACTION

1.2.1 Fundamental Principles of Neutron Diffraction

Over the past few decades the increased proliferation of neutron sources worldwide has seen the development of new techniques that take advantage of the unique properties of neutrons in order to provide insight into a wide variety of material properties. The advantages of using neutrons stem from their basic properties. These include a de Broglie wavelength of the order of the interatomic distances in condensed matter which provides structural information. An energy comparable to that of many common excitation phenomena such that any inelastic scattering of neutrons results in a large energy transfer [1]. This implies that energy resolved detection of neutrons can provide an insight into the atomic forces within the solid. The neutron also has a magnetic moment which makes them sensitive to the arrangement of electron spins such that the energies of the magnetic excitations within the solid can be determined. Finally the neutron is uncharged, hence there is no coulomb barrier to overcome meaning neutrons can penetrate deeply into the sample and are scattered by the nuclear rather than the electronic structure of the solid. For example the attenuation of intensity for neutrons having a wavelength of 1.4 Å in aluminium is ~ 1 percent per

millimetre, whereas for the equivalent energy X-rays it is over 99 percent [2]. The high penetration of neutrons into materials has made them an invaluable tool for many industrial and engineering applications.

Quantum mechanics tells us that the wavelength of a neutron is inversely proportional to the magnitude of its momentum (de Broglie relation); in terms of the wave vector $\vec{k}$ which has a magnitude: $k = 2\pi/\lambda$ this can be expressed as:

$$\frac{h\vec{k}}{2\pi} = m\vec{v} \qquad (1.1)$$

Where h is Planck's constant (6.626 x 10^{-34} J·s), m is the mass of the neutron (1.675 x 10^{-27} kg) and $\vec{v}$ is the neutron velocity.

The interaction of a single neutron with a nucleus may be described in terms of a scattering cross-section σ measured in barns (1 barn = 10^{-28} m^2). If the neutrons trajectory happens to bring it within the effective cross-sectional area presented by the nucleus, then the neutron is scattered isotropically. This is in contrast to X-rays which preferentially scatter in the forward direction. The origin of these differences lies in the fact that the neutron wavelength is much larger than the typical cross-section of the nuclei with which it interacts, hence the nuclear centres can be considered as point scatteres. X-rays meanwhile interact with the electron cloud surrounding the nucleus which occupies a volume usually comparable in size to X-ray wavelengths; hence X-rays do not scatter isotropically. If we represent the incident neutron beam as a plane wave of unit amplitude, i.e. $e^{ik\vec{r}}$ where $\vec{r}$ is the position vector for the neutron, the probability of finding the neutron anywhere in space is the same. Since the scattered neutron wave is isotropic it can be represented as a spherically expanding wavefield of the form $(-b/r)e^{ikr}$; where the $(1/r)$ term accounts for the inverse square variation of the intensity with distance from the origin. b, known in quantum mechanics as the scattering length, depends on the strength of interaction between the incoming neutron and the nuclear centre. The negative sign of the amplitude implies that b must be positive for a repulsive interaction between the two particles [1].

If we assume that all nuclei remain fixed in space, so that the scattering nucleus is undisturbed after the interaction (i.e. there is no transfer of kinetic energy), then the collision is elastic. An elastic collision also implies that the magnitude of the neutron wave vector is unchanged after scattering.

The units for the scattering length are metres; this quantity can be used to define a cross-sectional area for the interaction, σ, of a neutron scattering from a single nucleus: $\sigma = 4\pi b^2$ [3].

For some nuclei b varies with the energy of the incident neutron; close to the energy required to form excited nuclear states a resonance frequency exists which gives rise to a complex valued scattering length. This is analogous to the anomalous dispersion phenomenon that is observed with X-rays and just as in the X-ray case the real part of b corresponds to refraction (scattering) of the neutrons whilst the imaginary part corresponds to the absorption of neutrons by the nucleus [4]. In most experiments however the energy of the incident neutrons is below that required for resonant effects to occur and so the scattering length can be considered to be real and independent of the incident neutron energy. In terms of the equivalent X-ray experiment we would describe this as a weak-phase object, i.e. one in which absorption is negligible.

In order to account for the observed diffraction of neutrons by matter, we must consider how the scattered waves from each of the individual nuclei combine. If instead of considering just a fixed lattice of nuclei we now allow the nuclei to move about an origin, then the interaction of neutron with the nuclei during scattering can also impart a change in energy and momentum. Such a collision is inelastic and will induce a change in the incident neutron wave vectors magnitude and direction. Through conservation of momentum, the momentum transfer to the nuclei is given by equation 1.1 as: $\frac{h}{2\pi}\vec{Q} = \frac{h}{2\pi}(\vec{k} - \vec{k}')$, where $\vec{k}$ and $\vec{k}'$ are the wave vectors for the incident and scattered neutrons respectively. The scattering vector $\vec{Q}$ is thus determined by the magnitude of the wave vectors for the incident and scattered rays and the angle through which the neutron is scattered. For a scattering event that is elastic $\vec{k} = \vec{k}'$ (fig 1.1).

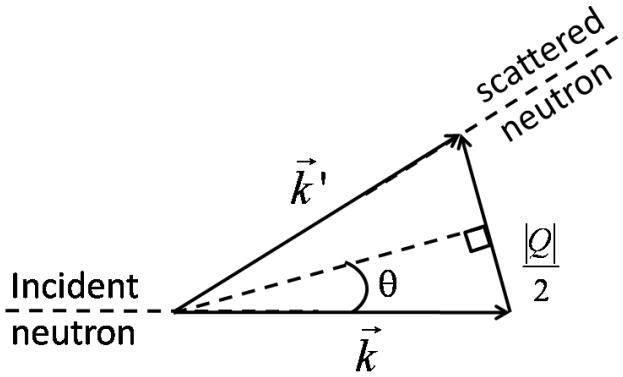


Figure 1.1: Schematic of elastic scattering event neutron energy and momentum remain unchanged after collision (adapted from reference [5]).

In terms of the scattering angle 2θ, $\vec{Q}$ can be defined as: $\vec{Q} = 2kSin\theta = 4\pi \sin\theta/\lambda$, if we define the energy transfer as ε, then the scattered intensity is just a function of these two variables normally denoted as $I(\vec{Q},\varepsilon)$ [6]. In 1954 Van Hove [7] was able to derive a general expression for the neutron intensity which is measured after scattering from an array of nuclei. This result was of fundamental importance to neutron scattering since it provided a simple means of relating (via the Fourier transform) the relative positions and motions of the nuclei to the scattered intensity. It is possible to decompose Van Hove's formulation to reveal two distinct types of scattering, these are 'coherent' scattering and 'incoherent' scattering. Coherent scattering is the form which is of most relevance to this thesis. For coherent scattering the waves scattered from different nuclei interfere to produce a superposition of wavefields which originate throughout the entire sampled volume. In other words it is a process which depends on the long range ordering/structure within the sample. The intensity distribution from coherent scattering contains fine-structure. Elastic coherent interactions are sensitive to the equilibrium structure of the sample, whereas inelastic coherent scattering contains information about the lattice dynamics. Incoherent scattering results when there is short-range order only, such that the scattered waves from different nuclei do not interfere (i.e. are not correlated) over any appreciable distance. The intensity distribution from incoherent scatter is just the sum of all the intensities for each individual scattering event.

1.2.2 Diffraction from Crystalline Solids

Diffraction is an elastic coherent scattering phenomenon; provided all the incident neutrons move at the same speed and along parallel paths they will all have an identical incident wave vector $\vec{k}$. When such a neutron beam is incident upon a fixed atomic lattice there will be no transfer of energy i.e. $\vec{k} = \vec{k}'$. The resulting spherical waves originating from each of the nuclear scattering centres will interfere constructively and destructively to produce a reinforced, amplified signal at well defined points in space (Fig 1.2). The symmetry/structure of the diffracted wave which is collected from the sample thus contains information about the lattice geometry and inter-atomic distances. The Van Hove formulation for diffraction from a periodic three-dimensional lattice composed of a single atom type is given as:

$$I(\vec{Q}) = \sum_{j,k} b_{coh}^2 e^{i\vec{Q}\cdot(\vec{r}_j - \vec{r}_k)} = \left\| \sum_j b_{coh} e^{i\vec{Q}\cdot\vec{r}_j} \right\|^2 \equiv S(\vec{Q}) \tag{1.2}$$

where $\vec{r}_i$ and $\vec{r}_j$ represent the position vectors for the *i*-th and *j*-th atom respectively and b_{coh} is the corresponding coherent scattering length for these atoms [7]. The quantity $S(\vec{Q})$ is known as the structure factor.

For large numbers of atoms the sum in Eq 1.2 is normally equal to zero since the spherical wavelets are out-of-phase. For a few values of $\vec{Q}$ however $S(\vec{Q})$ takes on a non-zero value. If we assume that the scattering vector projects perpendicular to a particular lattice plane and if the value of $\vec{Q}$ is a multiple of $2\pi/d$, where d is the spacing between atomic planes, then the argument of the exponential in Eq 1.2 must be a multiple of 2π, hence $e^{i\vec{Q}\cdot(\vec{r}_j - \vec{r}_k)} = 1$ if $\vec{Q} = 2\pi n/d$ [1, 8]. For all other values of $\vec{Q}$, $S(\vec{Q}) = 0$ and no intensity is observed at that scattering angle. Since the scattering vector can be readily defined as $\vec{Q} = 4\pi \sin\theta/\lambda$, equating this to the requirement that the exponential in Eq 1.2 be unity in order to observe diffraction we obtain the well-known condition for diffraction known as Bragg's law (originally demonstrated for X-rays) which relates the scattering angle 2θ, to the spacing between adjacent lattice planes:

$$n\lambda = 2d \sin\theta \tag{1.3}$$

In other words for constructive interference between the scattered waves from adjacent atomic planes to occur the path length difference between the incident and diffracted waves must be a whole number of wavelengths. From the Van Hove formulation the scattered intensity within each Bragg spot is proportional to the square of the density of nuclei within the scattering planes. This is evident from equation 1.2 which is the summation for all nuclei within each plane (j) of the unit exponential terms arising from constructive interference of the scattered waves. Hence the position of a particular Bragg peak allows us to determine the spacing between atomic planes whilst the intensity gives the density of nuclear scattering centres within the planes.

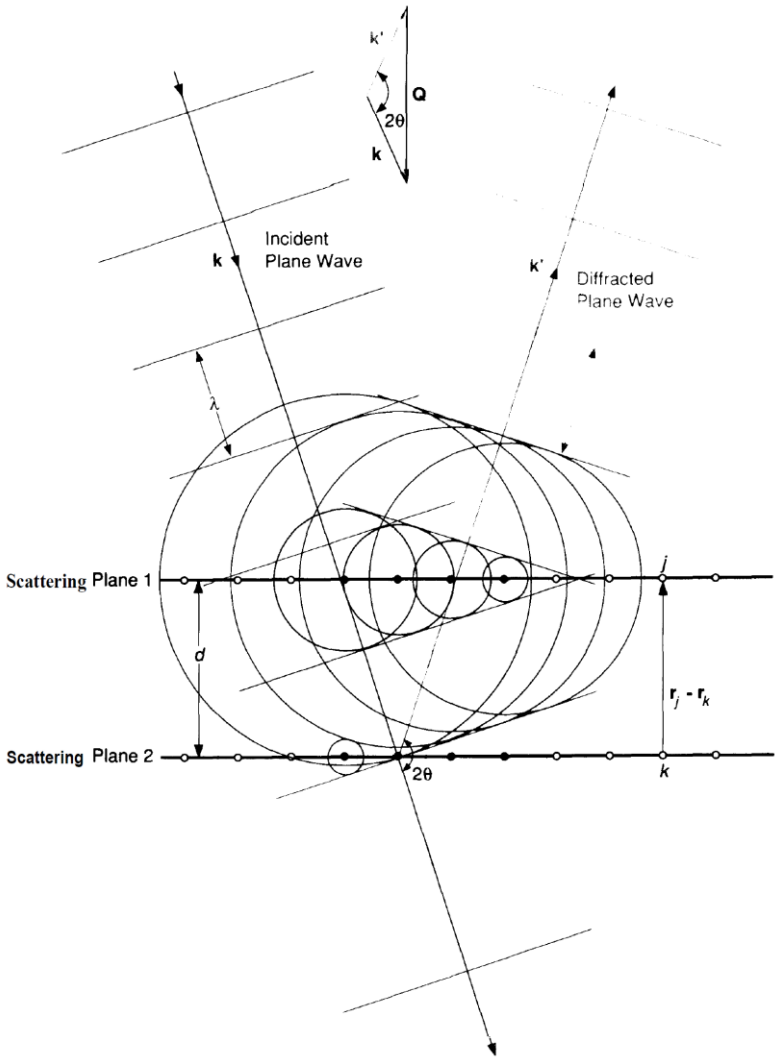


Figure 1.2: Neutrons incident upon a regular array of nuclei will scatter isotropically (represented by the spherical wavefronts). The outgoing waves interfere with one another, adding constructively only in particular directions, i.e. when Q is perpendicular to the scattering planes. In all other directions the sum of all scattered waves gives zero intensity (adapted from reference [1]).

For structures consisting of more than one type of atom, each atomic species can be considered to form a new set of crystallographic planes. If the d-spacing between each set of planes is different, the conditions for Bragg diffraction will also be different. The relative scattering power of each individual atomic species plus its relative position within the crystal's unit cell (the argument of the exponential in Eq 1.2) determines the contribution of each crystallographic plane set to a particular reflection. The intensity of each Bragg reflection therefore is determined by the type of atoms present and their position in the unit cell, whilst the position of the Bragg spots is set by the underlying symmetry of the crystal lattice [5].

1.2.3 Angle-dispersive neutron diffraction strain measurement

For measurements where strain needs to be determined in the bulk, conventional methods such as strain gauging and hole drilling cannot be applied. The most common technique employed to non-destructively determine strain within a sample volume is diffraction. These include neutron diffraction (discussed above), laboratory based X-ray diffraction, and synchrotron X-ray diffraction. Compared to laboratory methods synchrotron based diffraction offers increased flux and greater sample penetration, typically a few cm or more in aluminium, due to the higher energies available and also increased resolution. Neutron diffraction meanwhile affords the greatest penetration of all but normally at the cost of having a reduced spatial resolution and also a significant loss of intensity. As neutron diffraction is the most relevant to this thesis we will focus on this topic throughout the rest of the chapter.

The interpretation of diffraction strain data is still an area of active research and can be highly influenced by the experimental geometry and sample loading procedures. There are two principle modes for strain diffraction measurements, one involves the precise determination of the Bragg angle using a monochromatic incident beam, the other involves the use of a polychromatic beam and the determination of the energy of the Bragg reflection. The two modes are commonly referred to as angle-dispersive and energy dispersive respectively. Angle-dispersive mode is most often employed at continuous neutron sources whilst energy-dispersive mode works most effectively at pulsed sources (these sources are described in section 1.3).

In angle dispersive mode the underlying basis for strain determination comes from Bragg's law (Eq 1.3) in which changes in the lattice spacing are directly related to changes in the Bragg peak position. The main components of angle dispersive strain measurements are a monochromator, to produce a single wavelength beam, collimating system sample stages and detector (fig. 1.3). The stability of the set up strongly influences the accuracy of the determined strain values.

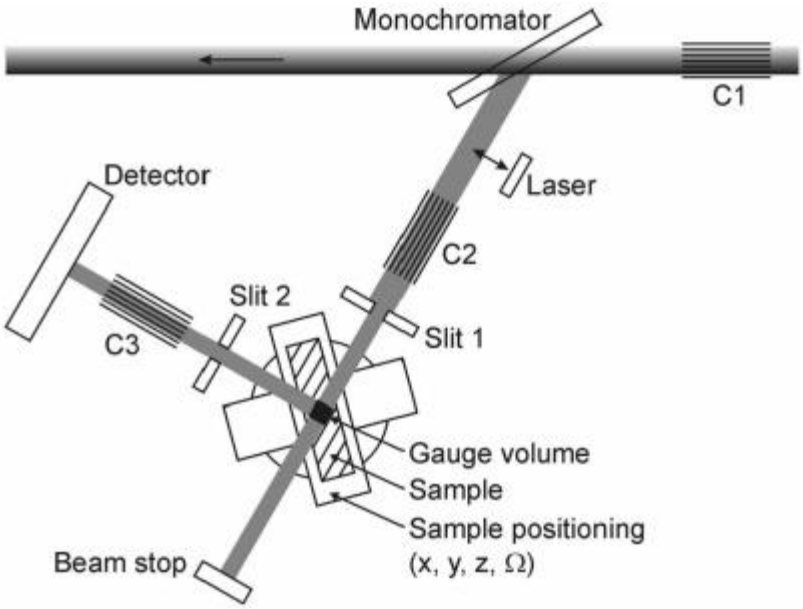


Figure 1.3: Typical set up for neutron diffraction strain scanning. The collimators C1, C2 and C3, define the divergence of the beam and thus the effective gauge volume within the sample.

To enable the selection of a single wavelength from the broad spectral distribution that is typical of neutron sources a perfect single crystal or mosaic crystal is used. The perfect single crystal approach to obtain a monochromatic beam offers some advantages in that no collimation is required post-monochromator. This is because the single crystal, normally perfect Si, can be elastically bent for controlled focusing onto the sample. When the radius of curvature is chosen such that is matches a specific diffraction angle a quasi-parallel beam emerges from the polycrystalline sample. In the case that the sample does not contribute significantly to the broadening of the measured diffraction peaks the broadening is largely determined by the thickness of the single crystal used to monochromatise the beam.

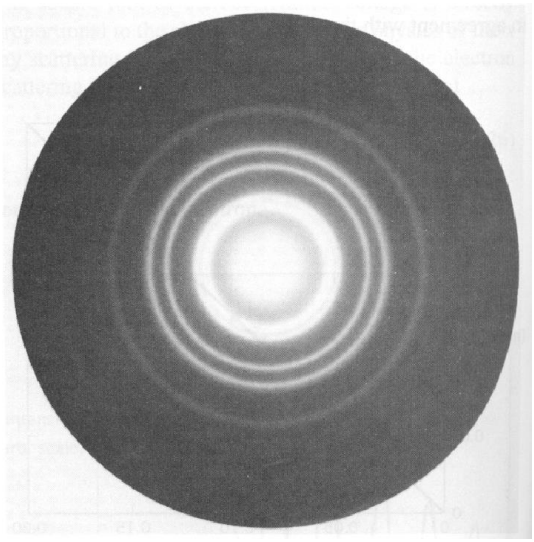
The alternative to single crystals is to use mosaic crystals; these contain large numbers of crystallites each having a slightly different orientation. This gives a much greater reflected intensity, since the Bragg condition is satisfied for more of the beam, however they also necessitate the use of collimators to obtain a well-defined gauge volume and thus spatial resolution on the sample.

The primary limitation on the resolution of the neutron strain scanning setup for the diffraction geometry shown in Fig 1.3 is the degree of collimation that can be achieved via the slit system used to define the size and shape of the gauge volume within the sample. The typical size of the incoming beam slits and diffracted beam slits is around 0.5 to 1 mm. This, combined with the

focusing of the monochromator, effectively limits the spatial resolution that can be achieved. The size of the gauge volume can be determined by scanning a wire through the beam close to the sample and measuring the diffracted intensity.

In carrying out angle-dispersive neutron measurements a number of assumptions need to be made, the first is that the diffracting grains within the gauge volume are representative of the entire sample. This can only be assumed however if a statistically significant number of grains are contained within the gauge volume. If the number of grains sampled is too small then the inhomogenities in the elastic properties of individual crystallites have a significant influence on the measurement. Hence the technique normally requires highly polycrystalline samples where enough grain orientations are included in each of the measurements that the experimentally determined strain value will be representative of the sample.

A perfect example of a sample suitable for angle-dispersive neutron diffraction would be a fine grained Ni-alloy, this has a typical grain size in the range of 5 microns and thus a large number of grains are contained within the gauge volume with each measurement. The resulting measured two-dimensional diffraction patterns represent slices through continuous homogenous diffraction cones, illustrated for a transmission geometry in Fig. 1.4a. However, as the sample becomes increasingly textured these rings break up into increasingly highly localised diffraction spots (Fig 1.4b). The errors on the stress values determined from highly-textured data are much larger than in the continuous diffraction ring case, often far exceeding the statistical measurement errors. There are three basic ways one can increase the number of grains sampled within the diffracting gauge volume of a highly textured sample, these are: rotating the sample during measurement, moving the sample in a lateral direction to the beam during measurement and increasing the size of the gauge volume. Each of these approaches however means that spatially resolved information for mapping the strain distribution within the sample is lost.



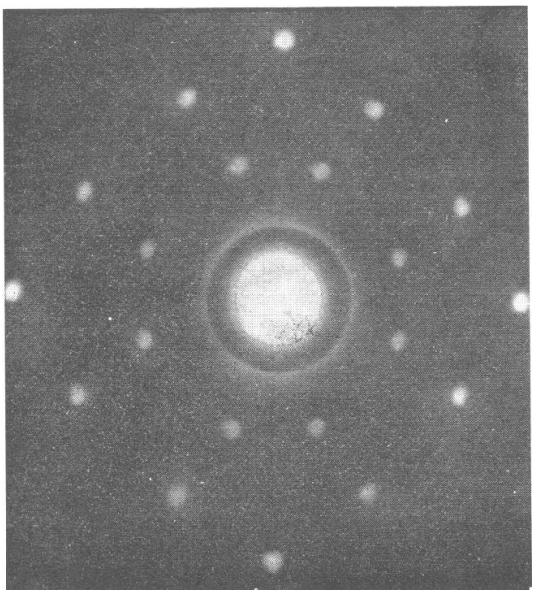


Figure 1.4a: (left) Neutron diffraction from a polycrystalline sample. **Figure 1.4b:** (right) Neutron diffraction from a highly crystalline sample, in this case sodium. Note that this data is taken in a transmission geometry.

A critical concern for neutron diffraction is the actual position of the sample in the beam; by scanning the sample laterally in the beam itself the position with respect to a single sample orientation can be determined. If the gauge volume is not fully contained within the sample bulk the result is an apparent shift in the diffraction peak position. To try to ensure complete immersion of the gauge volume within the sample a radial collimator is often employed.

For angle-dispersive neutron diffraction the data is collected by an area detector and hence is a two-dimensional matrix of intensity values. Variations in the detector pixel size and any apparent distortion in the alignment of the detector pixels will thus influence the accuracy of the measured strains. The first step in the data analysis is to convert the co-ordinates of the detector pixels into radial positions. Standard analysis approaches involve polar binning of the data to produce a single line plot of the diffracted intensity. For absolute measurements of the lattice constants it is necessary to know the wavelength of the incident neutrons to very high precision, however for strain measurements where one is generally concerned with relative changes this is less of an issue.

The measured diffraction peaks along the line profile are a convolution of the instrument resolution ('point spread') and the reflectivity of the diffracting sample. In many instances peak fitting simply involves fitting a Gaussian profile however in some cases where the sample structure

is such that very significant broadening occurs the peak shape can be much more complex. The subtraction of the background under the peak prior to fitting can usually be achieved with a simple linear or parabolic fit.

The measurement of elastic strain from angle-resolved neutron diffraction data is achieved via the following equation:

$$\varepsilon = \frac{d - d_0}{d_0} = -\frac{\theta - \theta_0}{\tan\theta_0} \tag{1.4}$$

where ε is the strain in the direction normal to the diffracting lattice plane, coincident with the scattering vector, and d_0 is the lattice parameter of a strain free portion of the sample. Strain is a second rank tensor with six spatially varying components, therefore at least six measurements of the sample along six different directions would be required to completely characterise the strain. In the case where the principle strain axes are known however, only the strain in these three perpendicular directions is required. For simple specimen geometries such as discs, tubes, and sheets the principle axes are assumed to coincide with the principle geometrical axes.

If we assume that the diffracting volume is isotropic and polycrystalline the residual stresses are calculated from the strains using the following formula:

$$\sigma_i = \frac{E_{hkl}}{1+\nu_{hkl}}\left[\varepsilon_i + \frac{\nu_{hkl}}{1-2\nu_{hkl}}(\varepsilon_1 + \varepsilon_2 + \varepsilon_3)\right] \tag{1.5}$$

where i =1,2,3 and the constants for the modulus of elasticity E_{hkl} and poisons ratio ν_{hkl} are given by their standard single crystal values which can normally be found in the literature.

The measured stresses consist of two components a hydrostatic and a deviatoric component. The hydrostatic part is the mean of the diagonal elements comprising the stress tensor whilst the deviatoric part is the deviation from the mean value in each of the six directions. If one is just concerned with calculating the deviatoric stresses then a value of d_0 is not required, in addition the effective Von Mises stresses can also be calculated without a precise reference.

1.2.4 Measuring a strain-free reference

One of the habitual problems of neutron diffraction as a technique to measure strains is the need to record the strain free lattice parameter, d_0. There are a number of challenges that need to be overcome when measuring an unstrained reference. The first is that the reference sample must be of the same chemical composition as the sample to be measured. This is an issue, for example, when determining the residual strain in weld joints as the heat treatment in the vicinity of the joint can strongly influence the chemical characteristics within the region which is affected by the heating. The most common means of obtaining a strain-free reference sample is to cut small blocks from the sample being investigated. The stresses within such small specimens are known to relax giving a nominally stress free reference. However the mechanical process of cutting out the reference block itself can also induce stresses which can propagate from the surface and into the bulk. Techniques such as electrical discharge machining generally induce smaller residual stresses in the reference material then conventional cutting. Depending on the sample, making use of stress balance or using the fact that the sample is 'thin' can also lead to a value for d_0.

1.2.5 Stresses at multiple length scale

The combination of stresses at the macro and micro scale leads to shifts in the peak position. Stresses at the macroscale are long range and continuous stresses within the sample; often in engineering it is desirable to measure only macrostresses which are the main factor in load bearing capacity. Trying to separate macroscopic stresses from microscopic ones however can be challenging. Microstresses often are the result of plastic deformation and can shift the peak position as well as cause peak broadening.

Microstresses are usually intergranular and have a varying influence on the different lattice planes due to the elastic anisotropy of the individual crystallites. Therefore, to isolate the influence of the macroscopic stresses alone reflections can be chosen for which the influence of the intergranular strains is small. In FCC materials for example the (111) or (311) reflections give the best approximation to the macrostresses. Similarly, with BCC materials the use of the (110) or (211) reflections minimises the effect of the intergranular stresses.

1.2.6 Future of angle-resolved neutron diffraction

Angle resolved neutron diffraction has been used as a means for determining stress for over 20 years. As such it has fully matured into a routine and useful tool for non-destructive residual stress mapping. The maturity of the method means that it is the principle tool used by industrial users and is regularly employed to measure strain within 'real' engineering components. Modern angle-resolved neutron strain facilities incorporate sufficient load bearing capacity to handle samples up to several hundred kilograms.

The recent availability of brighter neutron sources providing greater flux at the sample means the two- or even three-dimensional measurement of large samples is becoming an experimental reality. In combination with modelling work and a deeper understanding of the residual stress distributions inside samples this will lead to a more experiment driven design of engineering components.

1.3 Time-of-Flight Neutron Techniques

1.3.1 Time-of-flight Measurements

Spallation Neutron sources produce neutrons via the collision of high energy protons with a heavy metal target such as tungsten or uranium. The protons (or less commonly electrons) are produced from an accelerator coupled with a storage ring. The protons arrive at the target in short bursts (or bunches) which are typically less than a microsecond. Individual protons then collide with nuclei within the target driving neutrons from them. Neutrons produced via spallation can have energies up to tens of MeV [9]. Such high energy neutrons have wavelengths which are too short for diffraction from most materials; in addition they tend to induce damage to the atomic structure of the sample. Because of this neutrons must pass through a 'moderator' before being used for scattering experiments. Inelastic interactions with the atoms which make up the moderator reduce the energy of the impinging neutrons such that they emerge with the energy peaked around an average value determined by the moderator temperature. Moderating materials are those with a large neutron scattering cross-section such as water or liquid hydrogen.

Neutrons from a spallation source which have passed through a moderator typically have a broad distribution of energies (Fig. 1.5). Since, in contrast to reactor sources, neutrons from spallation sources arrive in pulses, the entire neutron spectrum is used as opposed to selecting out neutrons

of a particular energy. This is possible because of the fact that one can measure the time it takes for each neutron which is measured to travel from the moderator to the detector using a neutron spectrometer. The typical length of a neutron spectrometer is around 10 m, neutrons having an energy of 25 meV travel at 2200 m/s meaning they take about 5 ms to pass through the spectrometer [1]. Since the neutron pulses have a duration of ~10-20 μs the time taken for the neutron to pass through the spectrometer can be measured with relatively high accuracy. From these 'time-of-flight' measurements the neutron velocity and hence the neutron wavelength can be determined (from the de Broglie formula). Hence in neutron scattering experiments at spallation sources, for each detected neutron the time taken for the neutron to arrive at the detector is also recorded.

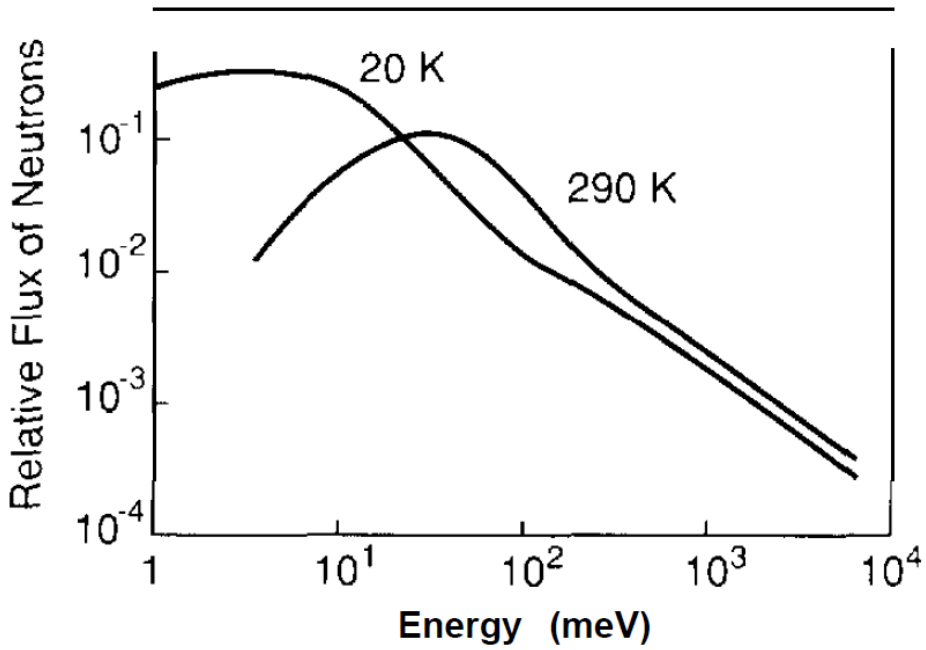


Figure 1.5: Typical neutron flux at a spallation source plotted as a function of energy for a water moderator held at 290 K and a Hydrogen one held at 20 K. Curves were produced at the Manuel Lujan, Jr. Neutron Scattering Center at Los Alamos (LANSCE).

1.3.2 Energy-dispersive neutron diffraction strain measurements

If the incident beam is polychromatic, that is containing a large number of different wavelengths, then for a fixed diffraction angle the Bragg condition is satisfied for a range of different lattice spacings. As described above, for a pulsed neutron source if the time of flight over a certain distance is measured then one can determine the energy of a given neutron. In Fig 1.6 an example of a time of flight neutron diffraction experiment is shown.

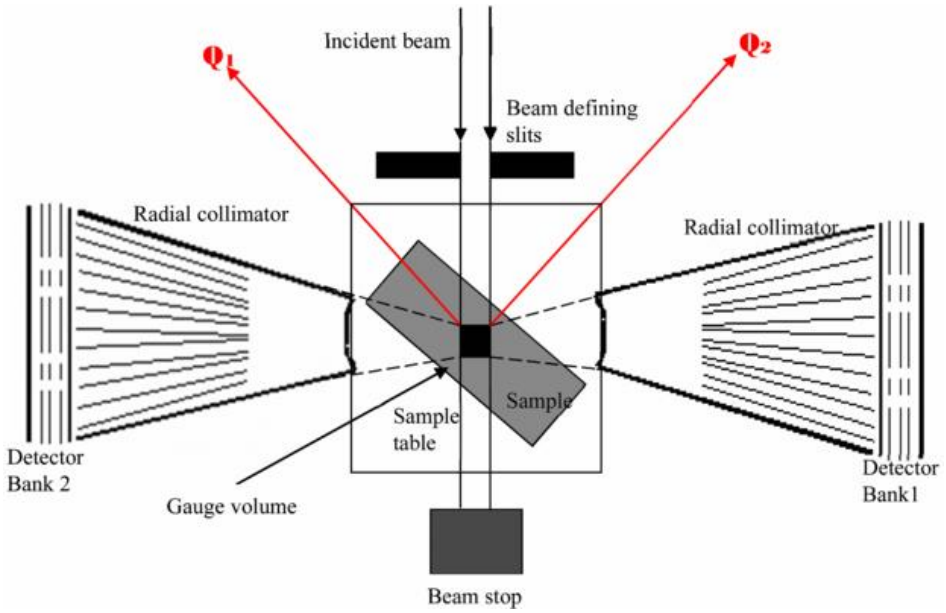


Figure 1.6: Experimental setup used for time-of-flight strain scanning at the ENGIN-X beamline, ISIS neutron facility. The incident beam is polychromatic.

If the initial time that the neutron leaves the source is defined as t_0 and the time it is recorded at the detector is t. Then:

$$t - t_0 = T = (L_1 + L_2)(m/2E)^{1/2} \qquad (1.6)$$

Where L_1 and L_2 are the distance from the source to sample and sample to detector respectively.

A multichannel time analyser is used to detect the incoming neutrons which are started simultaneously with each pulse emission. The number of recorded counts is thus stored as a function of the time each neutron takes to reach the detector. De Broglie's formula relates the energy and wavelength of the neutron via:

$$\lambda = h/mv = h/(2mE)^{1/2} \qquad (1.7)$$

where m is the mass of the neutron, v is its velocity, E its energy and h is Planck's constant. Equating E in 1.6 and 1.7, the time of flight, the total distance travelled and the wavelength are thus related by:

$$\lambda = hT/(m(L_1 + L_2)) \tag{1.8}$$

The moderation of the fast neutrons leading to a broad distribution of energies leads to an incident beam with a Maxwell-like thermal energy distribution. This gives each neutron pulse a characteristic shape - rising sharply at first but falling back down with a gentler slope. The typical width of one pulse is around 100 μs. The resolution of time-of-flight measurements is critically influenced by the width of the pulse as illustrated in Fig. 1.7. As it exits the moderator (position X_0) the beam contains a large spectral distribution, as the neutrons travel down the flight path the distributions corresponding to different wavelengths start to become slightly separated however they are still overlapping. After coming to the end of a long flight path (x_2) the different wavelengths become completely separated with respect to time.

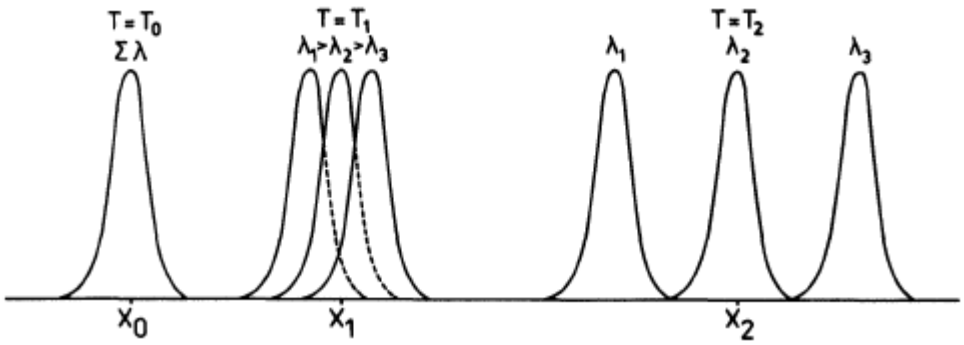


Figure 1.7: The influence of flight path on the separation of wavelengths in a polychromatic neutron pulse. At time $T=T_0$ the pulse contains all wavelengths, however after a short time the λ_3 neutrons have already edged in front passing point x_1 whilst the λ_2 neutrons are at x_1 and the λ_1 have not yet arrived at x_1. After travelling the whole length of the flight path ($T=T_2$) all three wavelengths are completely separated and do not overlap.

The longer the flight path the better the temporal, and consequently energy resolution for the incident beam. The caveat to this is that the longer the flight path the more intensity is lost in proportion to the inverse square of the distance travelled. To try to offset this, neutron guides are used; these utilise the total reflection of neutrons at metallic mirrors. However this in turn increases the divergence of the beam. The angle at which total reflection occurs is proportional to the wavelength of the incident neutrons so for longer wavelengths the use of neutron guides could be seriously detrimental to the resolution.

In time-of-flight energy dispersive neutron diffraction the Bragg angle θ is fixed and all allowed reflections are collected simultaneously. The measured intensity of the reflections is proportional to λ^4 therefore low index reflections will give a higher intensity and are preferred. In addition as the wavelength increases the resolution of the peaks also increases. Figure 1.8 shows a typical time-of-flight spectrum.

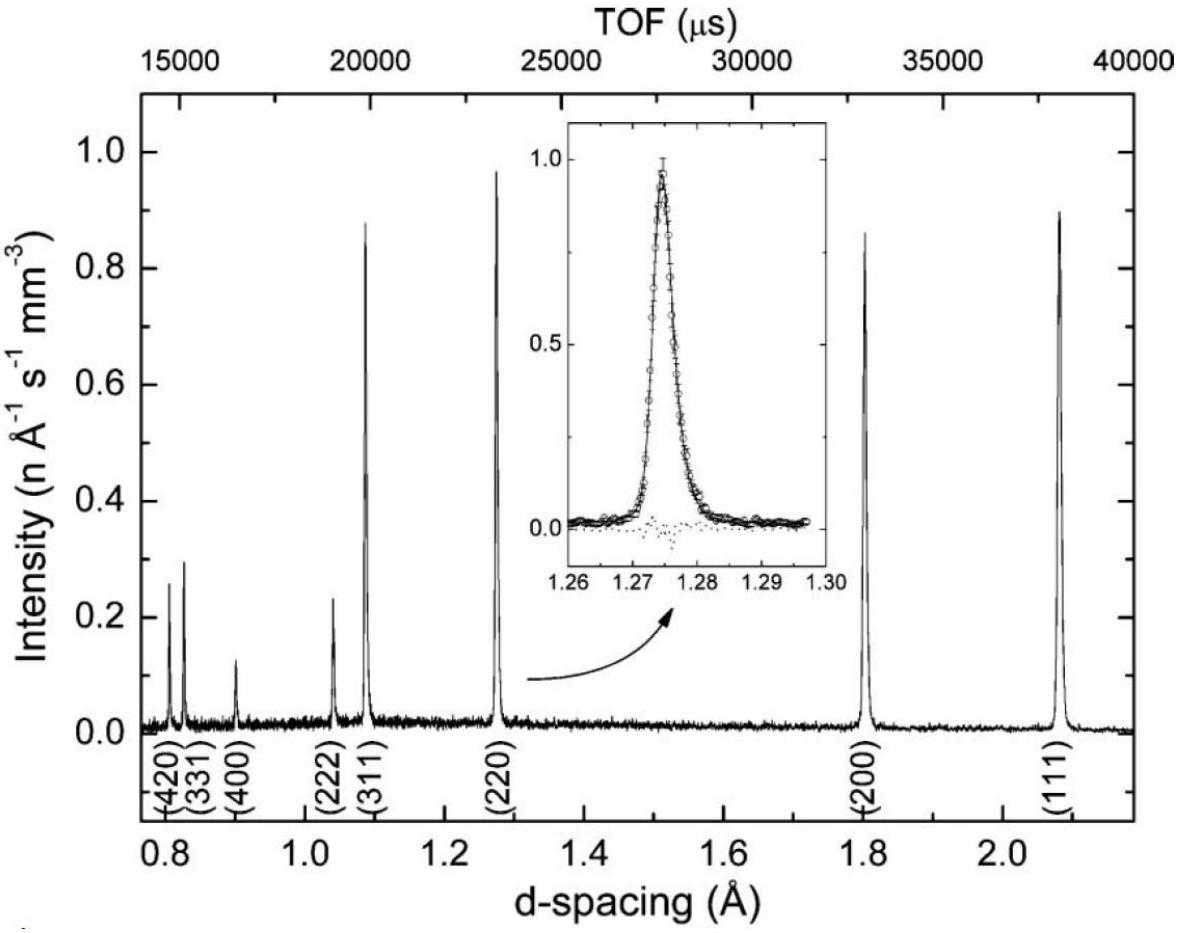


Figure 1.8: Time of flight spectrum recorded for stainless steel collected at ENGIN-X, ISIS neutron facility.

The peaks recorded in a time of flight spectrum each correspond to a different family of (hkl) crystallographic lattice places, thus the d-spacing is directly related to the peak position, t_{hkl}, in a time of flight spectrum.

$$d_{hkl} = \frac{h}{2\sin\theta m(L_1 + L_2)} t_{hkl} \qquad (1.9)$$

Least squares fitting is normally used to define the peak position. The typical sensitivities that one can achieve using time of flight neutron diffraction are of the order 50 με. As with angle-resolved neutron diffraction, changes in the spacing between lattice planes, d_{hkl}, with respect to the unstrained d_0 reference correspond to elastic strain.

Each individual diffraction peak in the time of flight spectrum only corresponds to the small number of crystallites within the diffraction gauge volume that fulfil the Bragg condition for that particular incident energy. The macroscopic strain, which is normally the critical parameter in engineering, is usually determined from the weighted average of a number of single-peak strains so as to increase the statistical significance of the measurement. The macroscopic strains can also be extracted from the time-of-flight spectrum by using Rietveld or Pawley refinements of the entire diffraction line profile.

1.3.3 Bragg-edge Neutron Transmission Measurements

For time-of-flight (TOF) experiments on polycrystalline materials (i.e. ones composed of many individual, randomly orientated, crystallites) characteristic edges appear in the transmitted intensity at energies corresponding to the individual Bragg reflections. Time-of-flight spectra are typically recorded as intensity versus neutron wavelength. For a particular d-spacing the scattering angle will vary depending on the wavelength according to Braggs law (Eq 1.3). As the wavelength increases, so does the scattering angle until a point is reached where 2θ equals 180 degrees, i.e. $\lambda = 2d_{hkl}$, where the subscript *hkl* refer to the miller indices used to identify the particular set of crystallographic planes contributing to that reflection. Beyond this point crystallographic planes having this *hkl* d-spacing no longer satisfy the Bragg equation, hence a sudden increase in the straight-through intensity is observed due to the previously diffracted component of the incident beam now being transmitted [10]. An example of the Bragg-edges observed for iron powder is shown in Fig. 1.9.

1.3.4 Strain Imaging using Bragg Edge Transmission

Each Bragg edge has as its origin a particular set of lattice spacings within the crystalline solid being measured. Any change in the wavelength at which a particular Bragg edge occurs therefore indicates a change in the lattice spacing of the planes, normal to the beam, which give rise to that Bragg edge. Just as with X-ray diffraction the planes of atoms within the crystal can be used as an internal strain gauge to indicate areas of fatigue or wear. Since a relative displacement in the position of the Bragg edge may be equated with a change in the lattice spacing, the strain may be

determined directly from: $\varepsilon = (d^{hkl} - d_0^{hkl}) / d_0^{hkl}$ in the direction collinear with the beam. Since, unlike XRD, the strain is determined from a direct transmission measurement in two dimensions a 'strain radiogram' analogous to the familiar absorption radiogram, may be constructed. In order to make spatially resolved two-dimensional strain measurements a segmented energy-resolving detector is required. Such a detector is available on the Engin-X beamline at the ISIS neutron facility [11]. For conventional absorption radiography the recorded image is the integral of the absorption along each line path followed by individual rays travelling to the detector pixels. In Bragg-edge strain imaging the strain, which is determined from measurements within each detector pixel, is the *average* of all the strain contributions along that line. Therefore a strain radiogram represents a two-dimensional averaged projection of the strain within the sample.

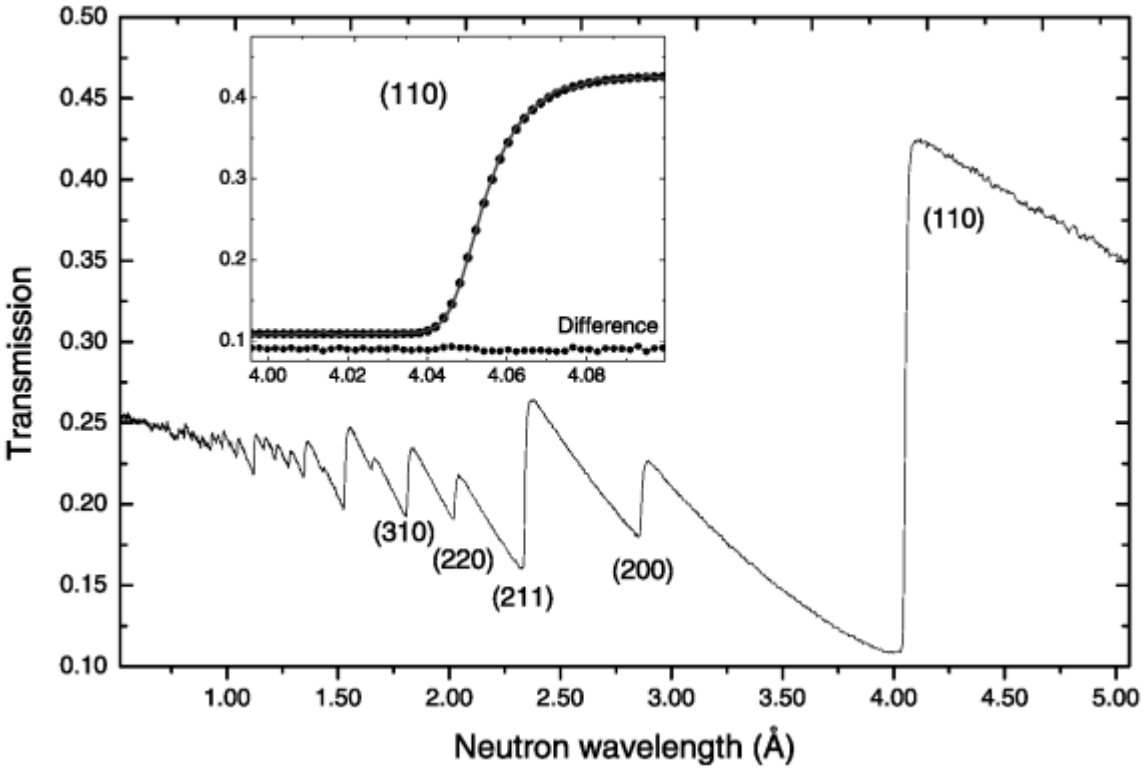


Figure 1.9: Measurements of the Bragg edges made from iron powder. Inset is shown a least squares refinement to determine the position of the (110) edge. Figure is taken from a paper by J. R. Santisteban et al. [10]

An example of a strain radiogram formed from Bragg-edge neutron data is shown in Figure 1.20. This data is for a cold expanded hole made in a 12 mm thick ferritic steel plate. If a hole is cold

expanded prior to insertion of a fastener it can increase the fatigue lifetime. Predicting the fatigue-life of these components relies critically on knowledge of the residual strain distribution within the material. The residual strain profile is clearly revealed in the Bragg-edge data analysis based on a single measurement using a two-dimensional pixellated detector.

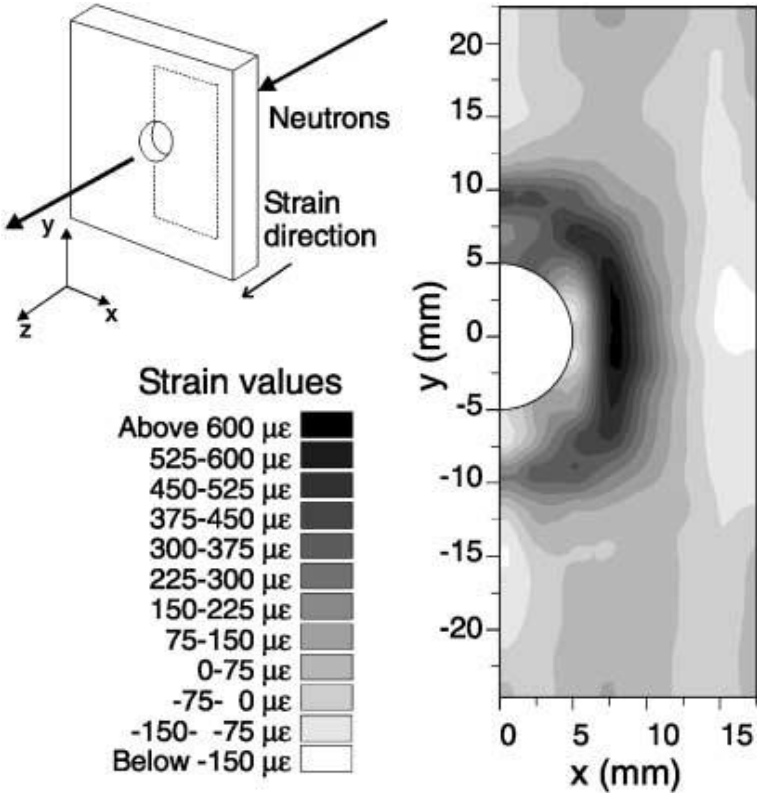


Figure 1.20: Residual elastic strain distribution in the direction of the beam around a cold expanded hole. Figure is taken from a paper by J. R. Santisteban et al. [10]

The essence of 'strain tomography' is to develop the necessary framework with which to deconvolve multiple averaged projections and thus obtain a three-dimensional distribution of strain throughout the sample. From a simplistic point of view the challenge here is exactly analogous to the problem of absorption tomography however the tensorial nature of the strain components in the present case significantly complicates the reconstruction process. Addressing these issues and assessing the feasibility of neutron strain tomography as a technique is the subject of this thesis.

1.4 REFERENCES

1. Pynn, R. (1990) *Neutron Scattering: A Primer*. Los Alamos Science.

2. Lovesey, S.W., *Theory of Neutron Scattering from Condensed Matter*. Vol. 1. 1984: Oxford: Clarendon Press.

3. Squires, G.L., *Introduction to the Theory of Thermal Neutron Scattering (2nd ed.)*. . 1996: .Mineola, New York: Dover Publications Inc.

4. Hecht, E., *Optics (4th Ed.)*. 2002: Addison Wesley.

5. Warren, B.E., *X-ray Diffraction*. 1990: Dover Publications Inc., New York.

6. Pynn, R. (1990) *The Mathematical Foundations of Neutron Scattering*. **NSA Primer**.

7. Van Hove, L., eacute, and on, *Correlations in Space and Time and Born Approximation Scattering in Systems of Interacting Particles*. Physical Review, 1954. **95**(1): p. 249.

8. Kittel, C., *Introduction to Solid State Physics, 8th Edition*. 2004: Wiley Book Publishing.

9. Zhang, S.H., *DPhil Thesis*, in *Engineeing Science*. 2008, Oxford.

10. Santisteban, J.R., et al., *Engineering applications of Bragg-edge neutron transmission*. Applied Physics A: Materials Science & Processing, 2002. **74**(0): p. s1433-s1436.

11. Santisteban, J.R., et al., *Comparison of Bragg-Edge neutron-transmission spectroscopy at ISIS and LANSCE*. Applied Physics A: Materials Science & Processing, 2002. **74**(0): p. s1616-s1618.

The Development of Neutron Strain Tomography

CHAPTER 2

2.1 Introduction

The previous chapter discussed the physics underlying the formation of Bragg-edges that enable 'strain radiograms' to be produced. The present chapter describes how average measurements of the strain derived from these Bragg-edges can be used to determine spatially resolved values of the elastic strain tensor. Firstly, the limitations of current methods for determining strain and the motivation for the development of neutron strain tomography are presented. Following on from that, the fundamental principles of inverting the average strain data and the possibilities for reconstructing the residual elastic strain profiles are summarised.

2.2 Motivation for Neutron Strain Tomography

In order to make predictions about how engineering components and materials behave under particular circumstances during their lifetime, the knowledge of residual elastic strains induced within the component during its manufacture is essential. Complete characterisation of the strain state within the sample requires a measurement of the six independently varying components which make up the strain tensor. The principal means via which the strain tensor has been evaluated experimentally in the past is through high-energy X-ray or neutron diffraction [1, 2]. These techniques are routinely used today to map the strain state of small engineering components and coupons from larger components in order to predict how they will behave under operational conditions during their lifetime.

Experimental measurements of strain are usually made by mapping in two dimensions. Measurement involves raster scanning a small beam across the sample to build up a spatially

resolved map of one of the strain components. The beam must be small in order to achieve a high spatial resolution for the image. In order to map additional components of strain, the sample must be re-oriented with respect to the beam. In all cases it is reasonable to assume that in an experiment, provided aberrations from partial filling of the gauge volume are avoided, the measured value of residual strain represents the *average* of all contributions to the strain within the scattering volume probed by the beam.

For many samples the crucial information about the residual elastic strain may be buried deep within the bulk. Hence, a two-dimensional through-thickness average measurement of the strain may not reveal, for example, the point of expected failure within the component. In order to build up a three-dimensional map of the component's strain state it is necessary to collimate the incoming and outgoing beams to define a particular scattering volume within the sample. However, the time then taken to map a sufficient number of sample voxels (three-dimensional pixels) renders high-resolution measurement of large volumes impractical.

The smallest spot size, and thus the highest resolution, that can be achieved at modern neutron and synchrotron facilities through either focusing or collimation is of the order of mm (neutrons) or microns (X-rays). Strain determination via either neutron or X-ray diffraction relies on the measurement of peaks produced by the constructive interference of rays reflected from specific sets of lattice planes. The Bragg formulation directly relates the angle at which these peaks are detected to the spacing between atomic planes, for a fixed incident beam wavelength. Thus, by comparison of the measured lattice spacing with the unstrained value, lattice elastic strain can be extracted.

Because of the need to raster the sample and to re-orient it with respect to the incident beam, experimental strain determination, particularly for large samples, is extremely time consuming. Hence there is a pressing need for non-destructive strain analysis of whole components to be made significantly more efficient, particularly with a view to three-dimensional strain imaging. The solution which we propose here attempts to reconstruct the various strain components using tomographic techniques [3, 4]. As with absorption tomography, the basic principle is to try to determine the strain tensor spatial variation from a redundant set of lower order projection data.

2.3 FUNDAMENTAL PRINCIPLES

In order to lay the foundations for the strain tomography reconstruction algorithm, let us first consider the sample to be composed of a two-dimensional matrix of unknown strain states that are to be reconstructed. For simplicity we restrict our discussion here to the two in-plane components of the strain only, i.e. we essentially assume that the sample extends in one dimension far out of the measurement plane, and that the out-of-plane components of the strain tensor are constant (generalised plane strain state). Each element in our matrix of unknown strain states thus represents a two-dimensional tensor quantity. It is worth noting here that when only one component contributes to the measurement (as is the case with some instances of X-ray strain tomography, [4]) the problem is reduced to a much simpler one since the measured strain may then be taken as the average of the strain values along the path of the beam; and standard inversion techniques suitable for scalar quantities can be readily applied.

For a circular sample it is most convenient to define the in-plane strain components in terms of components in the radial direction (perpendicular to the sample's lateral surface) and hoop direction (parallel to the sample lateral surface). For a parallel neutron beam incident on a circular cylinder sample and the transmitted beam measured by a pixellated detector, the situation is shown schematically in figure 2.1.

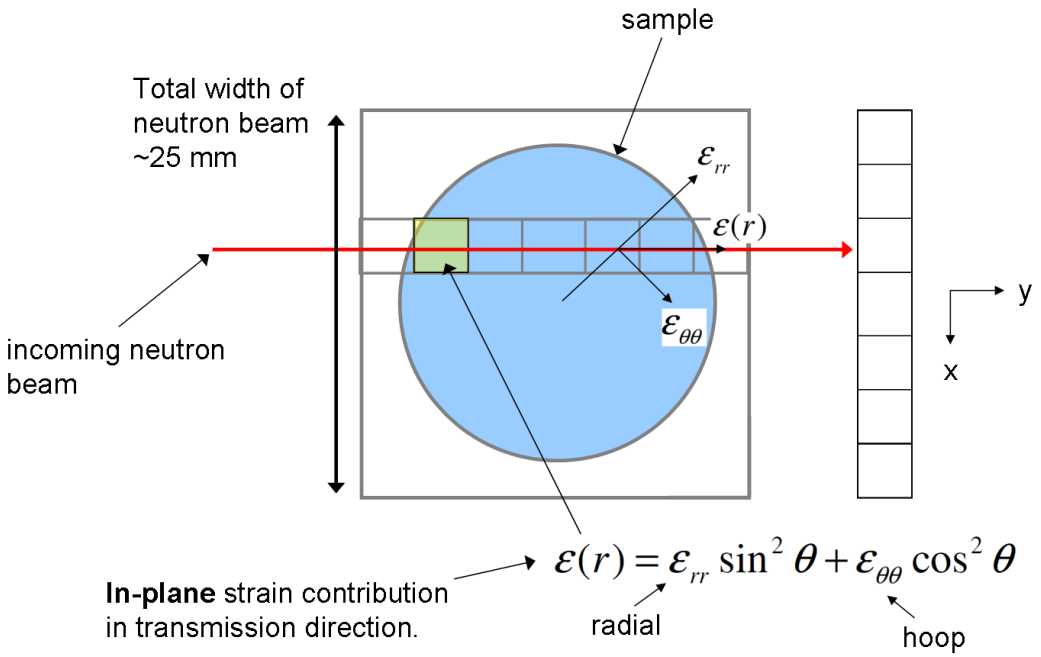


Figure 2.1: Schematic diagram of a parallel beam incident upon a circular cylinder sample (top-down view) for the neutron transmission measurements.

To isolate the component of strain parallel to the beam we need to apply the coordinate transformation rule to the strain tensor (fig. 2.2). Specifically, if we assume that the strains in the (x', y') coordinate system are known, we want to express the strain components in the (x, y) coordinate system. We would then like to use the strain component in the y-direction (parallel to the incident neutron beam) as this is the only direction for which the change in the crystal lattice interplanar spacing has an effect on transmission Bragg edge measurement.

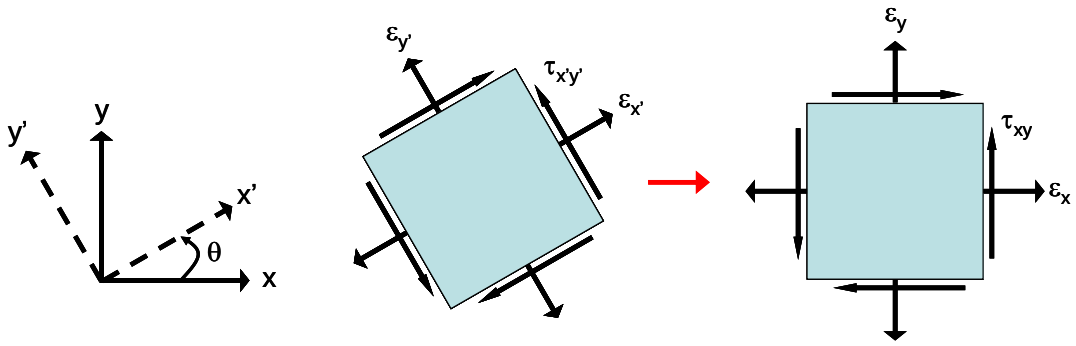


Figure 2.2: Rotation of axes in two dimensions representing the transformation of strain tensor components.

The relevant formulae for the transformation of strain may be derived by first considering the stresses within a small section of the sample in static equilibrium (fig 2.3) [5]. If P is a point within the sample and BC is a plane parallel to the z-axis, then at a small distance from P, together with the x-z, and y-z planes, a small triangular prism PBC is described. Assuming the specimen to be very small allows us to neglect the variation of stresses over the specimen and means that the stress can be assumed to be uniformly distributed. The forces acting upon this triangular section can therefore be determined by taking the product of the stress components and areas of the sides (neglecting shearing stress, which is justified, provided the principal axes are involved).

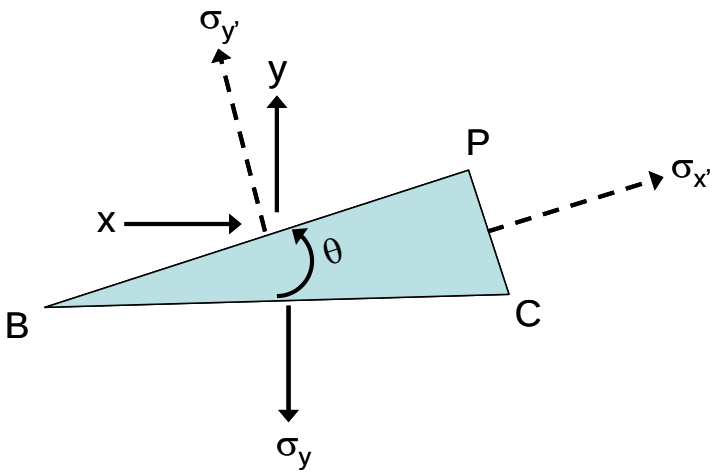


Figure 2.3: Triangular specimen in static equilibrium.

If the area of the side $BC = A$, then it follows that the area of $BP = ACos\theta$, and the area of $CP = ASin\theta$, where θ is the angle relative to the positive *x*-axis. Hence, balancing the forces in the y-direction:

$$(\sigma_{y'} Cos\theta) \cdot A\cos\theta + (\sigma_{x'} Sin\theta) \cdot ASin\theta = \sigma_y \cdot A \qquad (2.1)$$

Or upon re-arrangement:

$$\sigma_y = \sigma_{y'} Cos^2\theta + \sigma_{x'} Sin^2\theta \qquad (2.2)$$

This expression can also be used to calculate the strain transformations for $\varepsilon_{x'}$ and $\varepsilon_{y'}$ (this derivation can be carried out using simple geometric arguments) and re-written in matrix form as:

$$\begin{Bmatrix} \varepsilon_x \\ \varepsilon_y \end{Bmatrix} = \begin{bmatrix} c^2 & s^2 \\ s^2 & c^2 \end{bmatrix} \begin{Bmatrix} \varepsilon_{x'} \\ \varepsilon_{y'} \end{Bmatrix} \qquad (2.3)$$

Here $s = Sin\theta$, $c = Cos\theta$ and ε_x, ε_y are the components of the radial ($\varepsilon_{rr} = \varepsilon_{x'}$) and hoop ($\varepsilon_{\theta\theta} = \varepsilon_{y'}$) principal strains respectively, aligned with the detector axes.

So, by analogy with equation 2.2. the strain component in the transmission direction is given by:

$$\varepsilon_y = \varepsilon(r) = \varepsilon_{rr} Sin^2\theta + \varepsilon_{\theta\theta} Cos^2\theta \qquad (2.4)$$

Naively, one might assume that in the worst case scenario, a perfect knowledge of one of the in-plane strain components at every point in the sample would reduce the problem one of determining a single d.o.f. per voxel, and thus make the strain tomography problem tractable by standard techniques, e.g. filtered back projection. However, because of the spatially varying admixture of the components defined by equation 2.4, knowledge of *both* principal strain components at each position within the sample is vital.

Figure 2.4 illustrates the relative contribution from the in-plane strain components to the transmission direction strain. Fig 2.4a shows how the relative contribution of the in-plane strain components to the strain in the transmission direction varies depending on the position within a cylindrical sample. Fig. 2.4b shows how these components contribute to the average "transmission strain" which is measured at the detector. In the centre of the sample the measured strain depends only on the radial component, whilst at the edge of the sample it depends only on the hoop component. Trying to reconstruct the unknown hoop and radial strain components using measurements of the average transmitted strain therefore is a far more complex problem than that of absorption tomography.

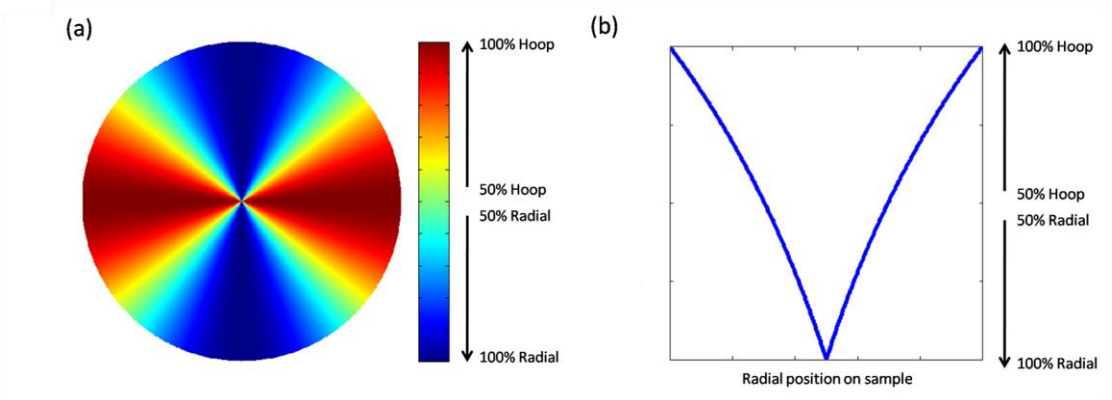


Figure 2.4: (a) Spatially resolved contribution from in-plane strain components (radial and hoop) to the transmission strain across cylindrical sample. (b) Contribution of each component to average strain measurement in the transmission direction.

In summary, depending on the beam position on the sample (and detector), either just the hoop or the radial or some mixture of both components may contribute to the measurement. There are residual strain components at certain positions within the matrix of unknown strain values to which we are not sensitive in any given transmission Bragg edge measurement. Therefore, either a connection must be made between the strain components on the basis of the solid mechanics principles, or some simple analytical model must be assumed for the unknown strains. Otherwise one would have to conclude insufficient strain information is available to regularise the problem and achieve reconstruction of the unknown strains.

The remainder of this chapter is devoted to describing the three approaches that have been applied to reconstructing the radial and hoop components of residual elastic strain from Bragg-edge neutron transmission data.

2.4 Strain Tomography

2.4.1 Introduction

The aim of all tomographic imaging, whether in the conventional absorption case or in the present case of strain tomography, is to reconstruct a three dimensional distribution from a set of lower order two dimensional data. Apart from papers published during the present study, there are two pieces of work in the literature (both by Korsunsky et al.) in which strain tomography has been used to reconstruct residual elastic strain. In the 2006 paper the strain distribution for a cylindrical quenched cylinder was reconstructed assuming a simple parametric model for the unknown axial strain component [4]. In 2011 this approach was generalised to an arbitrary strain distribution using the filtered back projection algorithm [11]. Both of these two previously published approaches to strain tomography were demonstrated in the X-ray regime and have dealt with just a single strain component, such that there was no convolution issue [4, 6]. These two previous strain tomography demonstrations are summarised below.

2.4.2 Previous Approaches to Strain Tomography

The approach taken in previous work from 2006 [4] was to construct a parametric model for the unknown strain distributions inside the object. A fitting procedure is then applied to minimise the mismatch between the measured data and the model prediction by updating the parameters in the model with each iteration of the fitting. The model parameters which yield the best fit to the experimental data can then be used to generate the residual elastic strain distribution at any point within the sample.

In the first proof-of-concept experiment for strain tomography, the technique was used to determine the residual elastic strain distribution in a quenched cylinder composed of nickel superalloy (IN718). For the quenched cylinder the residual strain distribution is known to be axisymmetric and approximately parabolic as a function of radius. This is because after quenching, the surface regions of the sample experience compressive axial residual elastic strain whilst the core of the sample supports tensile residual elastic strain. The shape of the parabola is constrained by the requirement of stress equilibration. With this knowledge it is possible to formulate a simple model for the residual elastic strain profile in the cylinder with just a few constants to be determined via strain tomography.

This model-based approach obviously relies on the accuracy of the initial assumptions made about the nature of the object and its residual elastic strain distribution. For the case of the nickel-base superalloy quenched cylinder it was assumed that the residual elastic strain could be modelled as a function of the radial position within the sample only.

The functional form of the strain distribution of the quenched cylinder, $\varepsilon(r)$, was approximated by a simple power series:

$$\varepsilon(r) = \sum_{i=0}^{n} c_i \varepsilon_i(r) = \sum_{i=0}^{n-1} c_i r^i \qquad r \le r_{\max} \tag{2.5}$$

Here r_{max} denotes the radius of the quenched cylinder, n is the total number of terms to be included in the truncated series, and c_i denotes the unknown coefficients which need to be determined through fitting of the experimental data. A cylindrical polar coordinate system was used to define the problem (r, θ, z), where z corresponds the axial direction within the

cylindrical sample. The strain recorded on the detector is the average strain sampled through the gauge volume [9]. Therefore, to convert the radial strain distribution given in Eq 2.5 to an average strain distribution in the direction collinear with the beam, we use the following formula:

$$\bar{\varepsilon}(x_j) = \frac{\iint_{A_j} \varepsilon(r) dA}{\iint_{A_j} dA} \tag{2.5}$$

i.e. the average strain determined within a width x_j on the detector is the integral sum of all of the strain contributions within the gauge volume defined by x_j, normalised by the area.

Since we now have a means of determining a predicted average strain from a forward calculation based on trial values for the unknown coefficients c_i, we also have a means of estimating the residual elastic strain profile for the quenched cylinder by minimising the function G, given by:

$$G = \sum_{j=1}^{K} \left(\bar{\varepsilon}(x_j) - \varepsilon(x_j) \right)^2 \tag{2.6}$$

In essence, this is a restatement of the least squares fitting approach.

For the quenched cylinder, the form of the strain distribution was simple enough, so that it could be modelled via just two terms in the strain distribution, i.e.

$$\varepsilon(r) = c_0 - c_2 r^2 \qquad r \le r_{\max} \tag{2.7}$$

For the experimental data collection, energy-resolved X-ray diffraction was combined with Rietveld refinement. The principle of stress balance was used to determine the unstrained lattice parameter for the quenched cylinder in order to extract the experimental average strains. The quality of the resulting parameterised fit of the model strain distribution to the measured diffraction strains may be judged from Fig. 2.5.

In summary, this experiment enabled an extraction of the coefficient values in equation 2.7 via comparison with the measured diffraction strains. Within the model assumptions of the problem this information was sufficient to reconstruct the spatially resolved strain value at any point within the sample. This experiment thus represented the first time that an attempt had been made to determine the spatially resolved residual elastic strain distribution within the bulk from a set of lower order average strain data.

A more recent experimental development of the strain tomography technique was reported in 2011 [9]. In this experiment, angle-resolved X-ray powder diffraction was used to record the average transmission strains in an in-situ loaded dental prosthetic sample made from sintered polycrystalline zirconia. The resulting Debye-Scherrer powder rings were then 'caked' (subjected to polar binning) to enable equivalent line diffraction profiles to be extracted, lattice parameters determined, and strain components to be separated. The z-direction in the experiment was defined as the long axis moving down through the prosthetic (see figure 2.6). This axis corresponded to scattering along the vertical direction on the powder ring. Therefore, data within an angular range of 10° close to the vertical line of the powder ring was summed for the data analysis as this best reflects the bending response of the dental prosthetic under applied load simulating mastication.

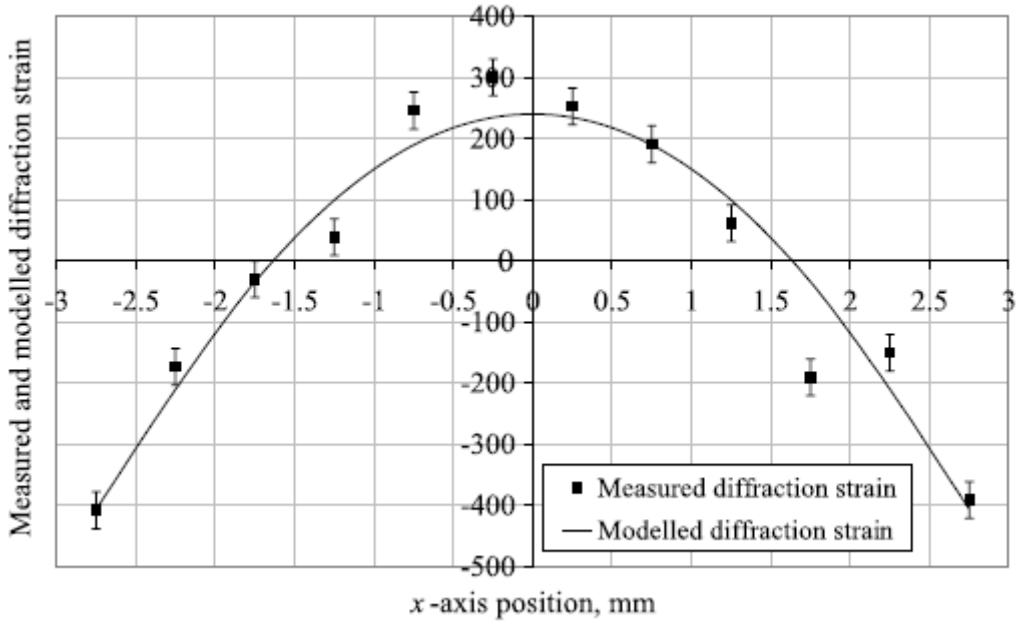


Figure 2.5: Comparison of model fit (solid line) to measured diffraction data for the nickel-base superalloy quenched cylinder [4].

For the data collection, a 1D line profile consisting of 57 scan points, with a 0.1 x 0.1 mm incident beam, was measured for each sample orientation after rotating around a vertical axis perpendicular to the beam every 3.6° over a total angular range of 180°. This is illustrated in Fig. 2.6. As the strain distribution in this case was unknown and non-axisymmetric, a different approach for reconstructing the strains to the one described above needed to be employed.

To reconstruct the strain distribution, a method was used that is much closer to that used for conventional absorption tomography, namely, the inverse Radon transform, also known as filtered back projection (FBP). In simple terms, given a 2D distribution of scalar values over an arbitrary area, the Radon transform performs the operation of summing up those values along one axis to give a 1D line profile and repeats this operation for a specified number of different orientations. The end result is a 2D matrix consisting of the 1D summed line profiles as a function of their relative orientation with respect to a fixed coordinate system. The Radon transform and its inverse are thus utilised in almost all absorption tomography, since the mathematical procedure described reflects closely the physical processes that take place in a standard tomography experiment.

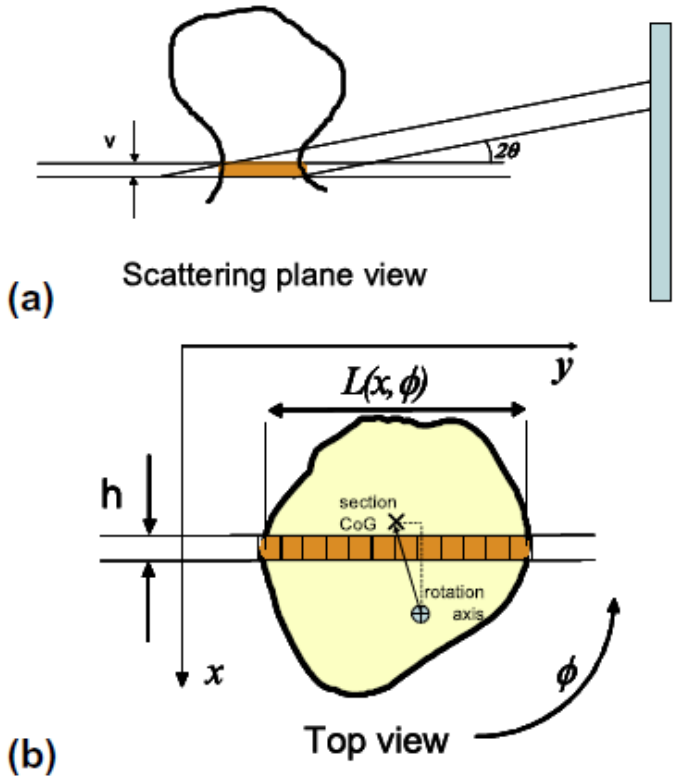


Figure 2.6:(a) The scattering geometry used to record the powder diffraction data [9]. The beam is incident from the left. The height and width of the beam define the scattering gauge volume, given by the orange shaded area. The measured strain obtained by fitting the diffraction line profile in the vertical direction represents the average strain throughout the volume traversed by the beam. (b) A plan view of the diffraction experiment. The sample is rotated in angle increments of 3.6° over ϕ = 0 to 180°. The rotation axis, which was not coincident with the centre of gravity for the sample, is shown on the schematic.

In this instance, we assume that we are measuring a single component of the strain only, i.e. just one component per sample voxel. Then the strain tomography problem in the dental prosthetic case may be thought of as taking the sum in the transmission direction (normalised by the path length) of the sample strains along a fixed axis of the sample. If this is then repeated for many different orientations of the sample, one obtains something akin to a sinogram, where the horizontal axis corresponds to the angle of rotation and the vertical corresponds to the position within the sample – in this case along the x-direction. For a single component strain measurement therefore, if we start with a 2D matix distribution of strains, take the Radon transform of this matrix and then normalise the result by the path length through the sample, we obtain the average transmission strains measured by the detector. This forms the basis for reconstructing the strains via direct inversion of the measured average strain data as a function of angle using the inverse Radon transform. Information about the path length in this experiment was obtained by performing a separate conventional X-ray absorption tomography experiment and matching the angles at which the strain tomography was taken to the orientation of the sample in the absorption tomography experiment.

The above method was applied to the powder diffraction data collected from the Zirconia dental prosthetic in the above case to give an estimate of the spatially resolved strain distribution. The results from this are compared to the finite element prediction for the strains within the dental prosthetic in Fig. 2.6. It can be seen that there is a reasonable match between the two sets of data, model and experiment, though the magnitude of the strains in both cases are not exactly the same and also the compressive region is not as well-defined in the strain tomography case. However, these differences were to be expected based on uncertainties in the experimental configuration, e.g. large fluctuations in the measurement of the applied load.

Both strain tomography cases dealt with so far in the literature share one key simplification. Namely, it is the fact that the analysis accounts for one of the six independent strain components only, along a single axis fixed with respect to the laboratory system. Within the present study we address cases in which multiple components of the stain tensor must be considered, and this presents a very different set of challenges. In the case where two components contribute to the measured strain and an obvious analytical solution is not available, some additional regularising constraints are required. For the neutron strain tomography problem, three different approaches have been developed. The basic theoretical framework for these approaches is described in the remaining part of this chapter.

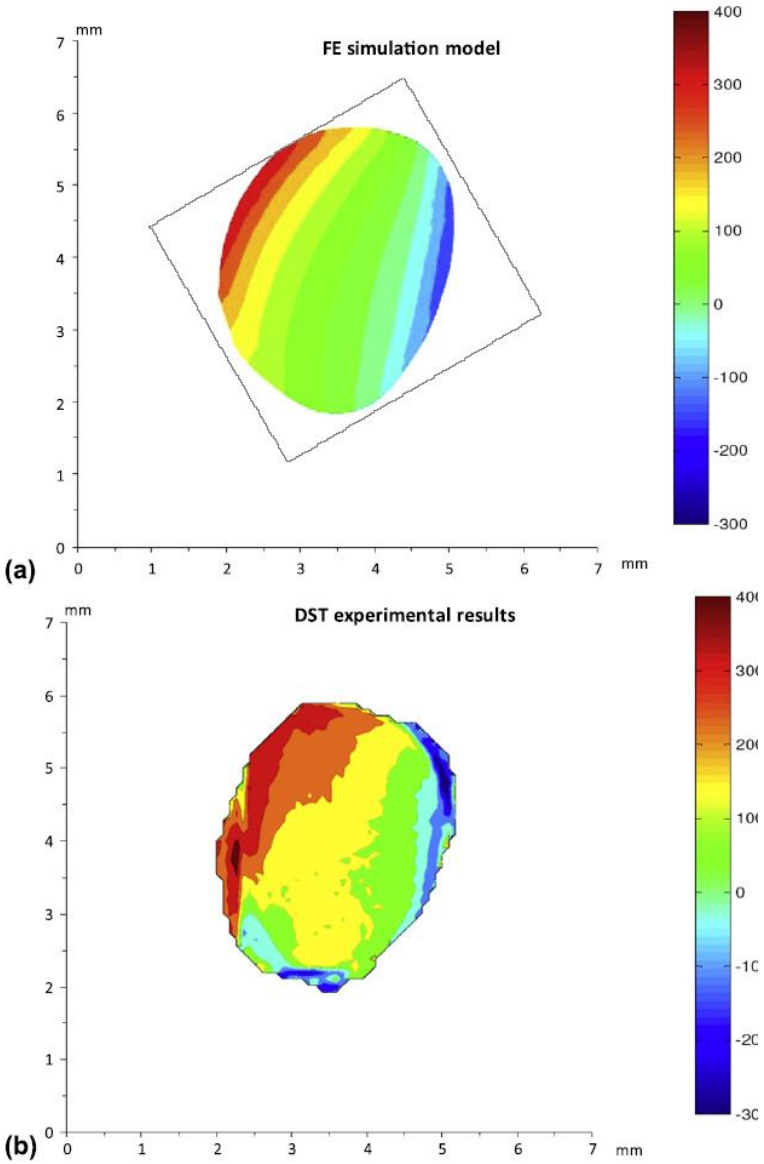


Figure 2.7: Comparison of the model strain calculated using Finite Element modelling to the distribution reconstructed using strain tomography [9].

2.4.3 Multi-Component Strain Tomography

The subject of the present work is neutron strain tomography based on measurement of the position of Bragg edges. The two published cases of strain tomography described above can only be applied when the measured signal arises from a single component of the strain tensor. In transmission Bragg edge measurements it is impossible, by any direct means, to isolate just one component of the strain which influences the measured data. Therefore, the aim is to regularise the strain tomography problem to deal with the fact that for a multi-strain component measurement there is more than one degree of freedom per sample voxel and thus, when compared to the cases above, the problem becomes ill-posed.

2.4.4 Linear Tent Function Representation

One approach to dealing with multiple strain components simultaneously is to construct a set of underlying basis functions to represent the unknown strain fields. Constraints on the allowed values for the strain may then be applied using a priori knowledge or fundamental relations such as strain compatibility through mathematical operations on the basis set. It also allows more qualitative constraints to be used such as enforcing a smooth continuous distribution. How this may be applied in practice and its ability to drastically reduce the uncertainty in the determination of the unknown strain distribution is discussed below.

One of the simplest functions that can be chosen to represent the unknown strains are so-called “tent functions”. These are highly adaptable functions giving rise to a piecewise linear representation of strain profiles and capable of increasing precision, as tent widths are refined. Depending on the circumstances, other functions may also be used as a basis set e.g. Legendre polynomials. However, tent functions afford an almost limitless flexibility in the type of distribution they can represent. To simplify the description without obfuscating the mathematical principles we will assume that the strain distribution is radially symmetric; such that the tent functions which we will use to represent the unknown strain can be defined as:

$$(r) = \begin{cases} 1 - r/w & 0 \le r \le w \\ 1 + r/w & -w \le r \le 0 \\ 0 & otherwise \end{cases} \tag{2.8}$$

Here *r* denotes the radial position of a field point and *w* denotes the tent half width. Adopting the polar coordinate notation introduced in section 2.3, we will use these tent functions to model the radial and hoop strain distributions.

Because of the radial symmetry of the problem, the tent functions in this case correspond to circular rings, as shown in figure 2.8.

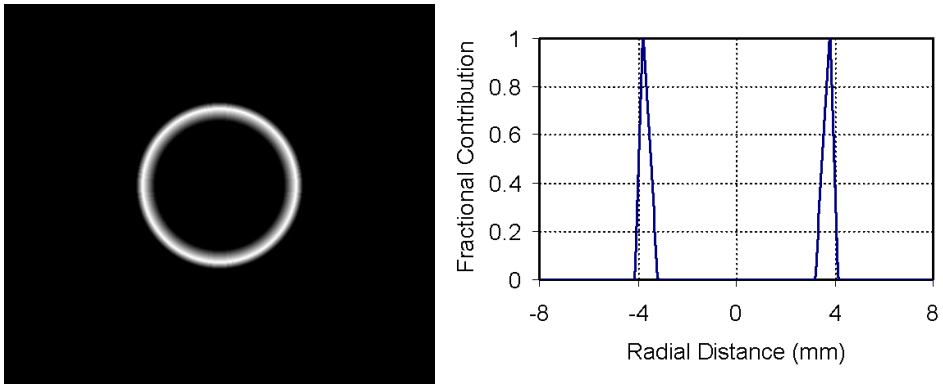


Figure 2.8: Radial tent function distribution (left) and corresponding lineout through centre of the function (right).

Between nodes the value of the tent function is a linear combination of the two neighbouring values for the strain. This stabilises the solution since none of the reconstructed strain values is entirely independent of the others. An example of the 1D tent functions used to represent the radial strain distribution measured from the quenched steel cylinder is shown in figure 2.9.

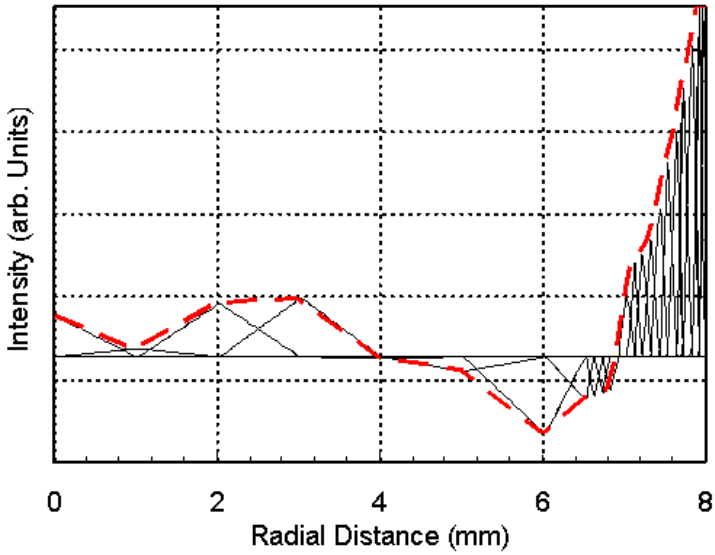


Figure 2.9: Representation of radial strain component from a quenched steel cylinder via 1D linear tent functions. Since most of the variation in the strains is expected at the edge of the sample the density of nodes is higher in this region.

The key challenge in neutron strain tomography is the resolvability of the multiple strain components with multiple degrees of freedom from projections of the strain field which have only one degree of freedom. One way of trying to address this is to reformulate the problem in terms of a single set of unknown variables by using fundamental results from solid mechanics linking the various strain components. To do this we propose to construct a set of basis functions that enforce the principle of strain compatibility. In polar coordinates, strain compatibility for the axially symmetric problems described here gives the following relationship between the radial and hoop strains [7]:

$$\varepsilon_{rr} = \frac{\partial u_r}{\partial r} = \frac{\partial}{\partial r}(r\varepsilon_{\theta\theta}) \tag{2.6}$$

By differentiation of the product of the tent functions representing the hoop strain distributions and the radial displacement a set of functions which implicitly satisfy strain compatibility can be formed. This allows the problem to be posed purely in terms of the hoop (or radial) strain component.

The strain component in the transmission direction is related to hoop and radial components via the following:

$$\varepsilon(r) = \varepsilon_{rr} Sin^2\theta + \varepsilon_{\theta\theta} Cos^2\theta = \frac{\partial}{\partial r}(r\varepsilon_{\theta\theta}) Sin^2\theta + \varepsilon_{\theta\theta} Cos^2\theta \qquad (2.7)$$

A coefficient matrix is formed from the product of the tent functions with the 2D $Sin^2\theta$ function (radial) or 2D $Cos^2\theta$ (hoop). The sum of the result along the transmission direction normalised by the path length gives the relative contribution for a particular node. By stacking the result for each node, *k*, the coefficient matrix is formed for both the hoop and radial components, i.e.:

$$\frac{\sum_{i=1}^{N_j} \Lambda_k(r) \cdot Cos^2\theta_{i,j}}{N_j} \qquad k = 1....L \qquad \text{(for Hoop component)}$$

$$\frac{\sum_{i=1}^{N_j} \frac{\partial}{\partial r}(r.\Lambda_k(r)) \cdot Sin^2\theta_{i,j}}{N_j} \qquad \text{(for Radial component)} \qquad (2.8)$$

Here N_j is the path length through the sample in the transmission direction which depends on the relative position in the *x*-direction. In order to account for the finite detector channel size (in this experiment this was 2mm), it is necessary to average the strain across the width of the transmission gauge volume within the sample, i.e. for:

$$(x_j - \Delta x/2) \le x_j \le (x_j - \Delta x/2) \qquad j = 1 \ldots J \qquad (2.9)$$

where Δx is the width of the detector pixel, x_j is the position of the centre of the sample with respect to the centre of the beam for each data point, and J is the total number of measurements. The result is a 2D matrix with L nodes defining the tent functions for the radial and hoop strains in one direction and the number of average strain measurements defining the other direction.

To determine the hoop strain profile (and thus through compatibility the radial strain profile), an iterative reconstruction procedure is carried out to find the solution which minimises the sum of squared differences between the forward calculation and the measured data, and also the

local point-to-point variation in the solution. Because of our particular choice of basis function, any solution for the strain *must* also be consistent with compatibility. The objective function is thus expressed as:

$$\|Ab - C\|^2 + \|\lambda D\|^2 \qquad (2.10)$$

Here in the first term, **A** is the coefficient matrix $[\varepsilon_{k,j}]_{LxJ}$,, *b* is the vector representing the hoop strain components, **C** are the measured strains $e(x_j)$. For the second term, λ is a weighting factor determined by the required 'smoothness' of the resulting fit for the radial strain component. This regularisation term is necessary because the gradient of the piece-wise linear tent functions is 'step-wise' discontinuous. In order to minimise the point-to-point variation of this step function, we use the mean gradient of the tent functions to construct the radial strain, and include a difference operator D in the minimisation given by $\varepsilon_{rr} - x_0$ where x_0 is a cubic smoothing spline fit to ε_{rr} [8].

2.4.5 Parameterised model approach

The first study demonstrating the principle of strain tomography summarised in section 2.4.2. used a simple power series model to represent the strain distribution in a quenched cylinder. The best fit of the model to the experimental data then yielded the coefficients in the power series and thus the value of the strain at any point within the sample can be found by applying this model. A similar approach can also be applied in the case when there are multiple strain components measured simultaneously. In this case, however, a separate parameterised model needs to be constructed for each of the components. The general functional form of each component may be similar, or it could be different depending on the particular case being investigated. This approach inherently relies on the use of a priori knowledge about the final form of the strain distributions in order to choose the correct functional form. A good guess at the approximate form of the strain distribution can often be obtained through finite element (FE) modelling. Once a function is selected to represent the experimentally extracted strains, the variables defined in the function may be determined via strain tomography.

An example of this method being applied for neutron strain tomography is given in [3]. In this study, a quenched steel cylinder was investigated in a way that is similar to the first X-ray strain

tomography experiment described above. FE simulations showed that the quenched cylinder strain distribution could be adequately represented by the exponential function multiplied by a truncated power series, given in equation (2.11):

$$\varepsilon(r) = \sum_{i=0}^{n} c_i \varepsilon_i(r) = \sum_{i=0}^{n-1} c_i \exp(r)\, r^i + c_n \qquad r \le r_{\max} \tag{2.11}$$

where c_i are the coefficients to be determined, $\exp(r)$ is the exponential function, $\varepsilon(r)$ are the strain components within the sample to be reconstructed and $r_{\max}$ is the external sample radius.

Through equation (2.7), the strain component in the transmission direction within each sample voxel is directly related to the radial and hoop strains. If we denote the average predicted strain on detector pixel, *j*, due to the basis function $\varepsilon_i(r)$, by $\bar{\varepsilon}_{ij}(r)$. We may then introduce the following definitions in matrix notation:

$$\mathbf{A} = \sum_{j=1}^{n} \bar{\varepsilon}_{ij} \bar{\varepsilon}_{ki}\ ,\ \mathbf{c} = \sum_{i=1}^{n} c_i \quad \text{and} \quad \mathbf{b} = \sum_{j=1}^{n} \bar{\varepsilon}_{ij} e(x_j) \tag{2.12}$$

where *n* is the number of unknown coefficients to be determined and $e(x_j)$ are the strains measured at points x_j in the detector plane. The equation relating the unknown coefficients to the measured strains is then given by:

$$\mathbf{Ac} = \mathbf{b} \tag{2.13}$$

Once the matrix $\mathbf{A}$ and vector $\mathbf{b}$ have been formed, the problem is reduced to one of solving the linear algebraic system of equations (9) for the unknown coefficients represented by the vector $\mathbf{c}$. In practice the system is usually over-determined since the number of unknown coefficients is relatively small compared to the amount of experimental data available. Solutions for $\mathbf{c}$ were again found using least-squares fitting, i.e. minimising the value of $\|\mathbf{Ac} - \mathbf{b}\|^2$ [3]. Once the values of the coefficients within the parameterised function have been determined from fitting the experimental data they may be used in combination with the function given by Eq. 2.11 to predict the strain at any point within the sample.

2.4.6 Combined Neutron Diffraction and Strain Tomography

A third possibility for deconvolving the in-plane strain components is to include a limited amount of neutron diffraction data in the calculation. The procedure to change between the time-of-flight neutron diffraction setup described in chapter 1 and the setup used for neutron strain tomography is relatively simple (see Fig 2.10). In the diffraction case the scattered signal on the detector orientated at close to 90 degrees with respect to the incident beam is measured using slits to define a small gauge volume. For the Bragg-edge measurements, a spatially resolved time-of-flight transmission detector is used. Hence, the two methods are highly compatible, though they differ in terms of spatial resolution. For the diffraction measurements just one of the principal axes is measured at one time, however, even with a few diffraction measurements constraining the solution, a very large benefit in terms of regularising the solution can be obtained. The results of this method being applied are given in chapter 3.

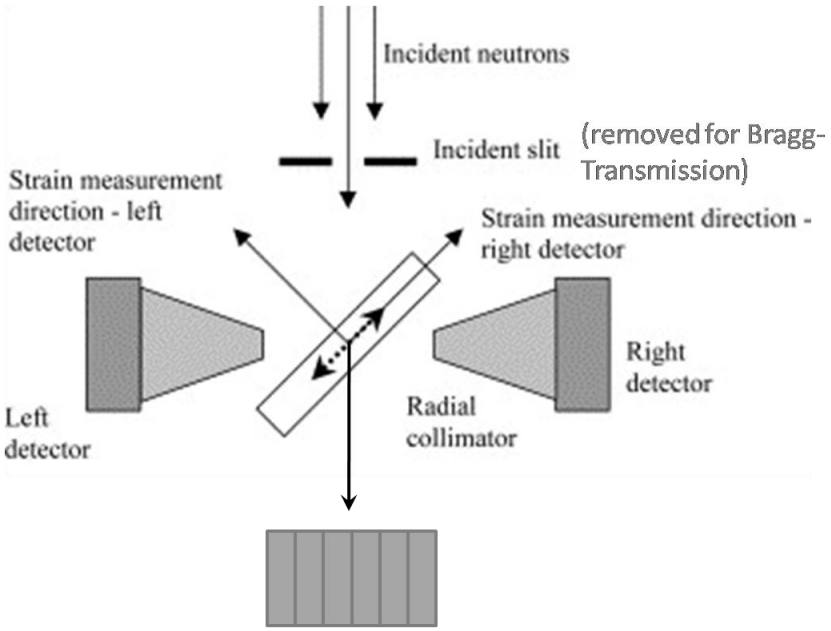


Figure 2.10: Experimental set up for combined neutron diffraction and strain tomography experiments. Switching between modes involves the removal of a single pair of (incident) slits.

Due to the fact that the strain components contribute by varying degrees to the measured average strain (see figure 2.4), it is not sufficient to have knowledge of just one component. The position within the sample of the components which need to be measured must be chosen carefully depending on their local relative contribution to the average strain. Preliminary results

have shown that, depending on the complexity of the strain distribution, a few well-chosen diffraction measurements can be used to determine the overall residual strain distribution from transmission measurements. Initially, a combination of neutron diffraction and Bragg-edge measurements is likely to be the most effective method of determining the three-dimensional residual strain profile. One of the key questions that need to be resolved through further experiments is the amount of diffraction data that needs to be collected in order to sufficiently constrain the possible values for the neutron strain tomography. Our results for axisymmetric strain distributions indicate that the inclusion of just two "point" diffraction measurements, one aligned with the centre of gravity of the sample and the other at the edge of the sample, is sufficient to completely regularise the strain tomography problem.

This chapter summarised the basis for the three main approaches applied to strain tomography. The next chapter will concentrate on the experimental results that have been obtained using this technique.

2.5 REFERENCES

1. Korsunsky A.M., Wells K.E., Withers P.J.,, *Mapping two-dimensional state of strain using synchroton X-ray diffraction.* SCRIPTA MATERIALIA, 1998. **39**(12).

2. Withers, P.J., M.W. Johnson, and J.S. Wright, *Neutron strain scanning using a radially collimated diffracted beam.* Physica B: Condensed Matter, 2000. **292**(3-4): p. 273-285.

3. Abbey, B., et al., *Feasibility study of neutron strain tomography.* Procedia Engineering, 2009. **1**(1): p. 185-188.

4. Korsunsky, A.M., et al., *The principle of strain reconstruction tomography: Determination of quench strain distribution from diffraction measurements.* Acta Materialia, 2006. **54**(8): p. 2101-2108.

5. Bower, A.F., *Applied Mechanics of Solids*. 2010: CRC Press, Taylor and Francis Group.

6. Daymond, M.R., M.W. Johnson, and D.S. Silvia, *Analysis of neutron diffraction strain measurement data from a round robin sample* The Journal of Strain Analysis for Engineering Design, 2002. **37**(1): p. 73-85.

7. Timoshenko, S. and J.N. Goodier, *Theory of elasticity*. 1970: Mc Graw-Hill.

8. Tychonoff, A.N. and V.Y. Arsenin, *Solution of Ill-posed Problems*. 1977: Washington: Winston and Sons.

9. Korsunsky A.M. et al., *Strain tomography of polycrystalline zirconia dental prostheses by synchrotron X-ray diffraction*, Acta Materiali 2011. 59(6), p: 2501-2513.

CHAPTER

EXPERIMENTAL RESULTS

3

3.1 INTRODUCTION

To demonstrate the feasibility of neutron strain tomography we have analysed the average 'projected' strain profiles from an aluminium shrink-fit "ring and plug" sample, a spray quenched cylinder, and a square cross section bent steel bar. The first two samples were chosen due to the radial symmetry of their bulk residual elastic strain distributions, thus providing proof-of-principle without requiring multiple measurements of the transmission strain. In this chapter we describe and contrast three different approaches for extracting the spatially resolved strain components [1]. The final plastically bent beam sample corresponded to more general, non-axisymmetric case.

3.2 SAMPLE PREPERATION AND MESASUREMENT

3.2.1 Literature Review: Samples

The first sample was a VAMAS (Versailles Project on Advanced Materials and Standards) round robin shrink fitted aluminium ring-and plug [2]. The outer diameter of the ring was 50 mm and the outer diameter of the plug was 25 mm. The ring-and-plug sample is shown in figure 3.1. This sample is an excellent test case for the strain tomography method. The sample has previously been characterised at 18 neutron facilities around the world using neutron diffraction techniques in order to establish the reliability of neutron diffraction as a method for strain measurement. The strains for the ring-and-plug sample were calculated as relative changes in the lattice parameter values with respect to the reference value obtained from a calibration measurement on a nominally stress-free sample of the same material.

The results from measurements at these facilities showed a consistency in the strain measurements of less than 100 με. The conclusions of the work of Daymond et al. were that shifts of these magnitudes are not statistically significant. The diffraction results in [2] were analysed by the authors using a Bayesian approach to give a 'mean' strain for each measurement point within the sample. These values are used as a comparison to the neutron diffraction data in this thesis.



Figure 3.1: Ring-and-plug test sample.

The second sample consisted of a stainless steel cylinder, 16 mm in diameter that had been subjected to water spray-quenching. Four 60° cone spray nozzles, equally spaced around the circumference of the cylinder were used to quench the sample after it had been heated to 800°C. The temperature of the spraying water was 80K. This treatment is known to give rise to residual stresses localised in the vicinity of the cylinder surface [3].

The measurements were performed at the ENGIN-X instrument at ISIS (RAL, UK) [4] by Dr Vorster, Dr Zhang and Prof. Korsunsky [3, 5]. The beam size was ~25 mm (vertical) × 25 mm (horizontal). Spectra were recorded on a 2D pixellated area detector with an array of 10 × 10 scintillation detectors, each 2 × 2 mm^2 in area and placed on a 2.5 mm pitch. To increase the measurement resolution and to record data from the entire sample volume, the sample was scanned perpendicularly to the beam (*x*-direction). In transmission, the strain determined from measuring the position of the Bragg edge gives the average strain component in the direction

parallel to the incident beam. The experimental setup for the transmission neutron measurements is shown in figure 3.2.

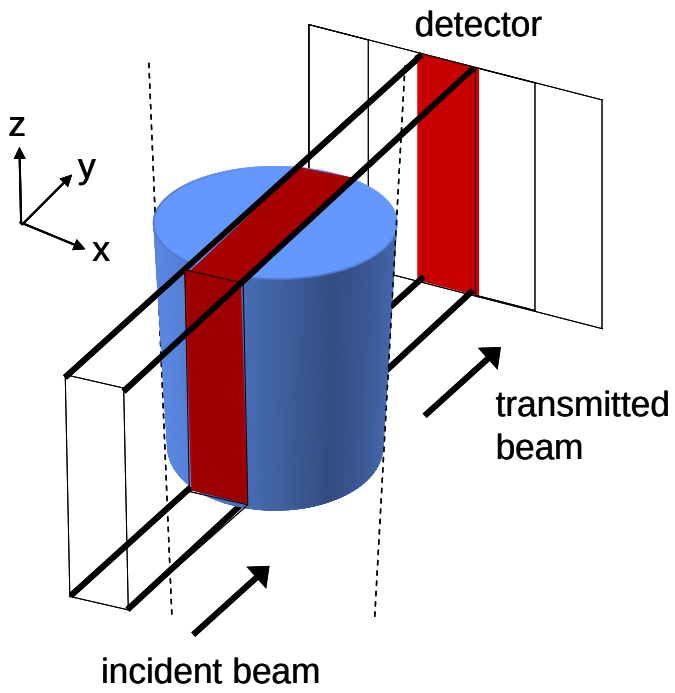


Figure 3.2: Schematic of the experimental setup for the neutron transmission measurements. The highlighted gauge volume represents the portion of the sample irradiated by the neutron beam. Also shown is the column of pixels of the area detector from which the transmission data was collected at each step of the sample translation in the *x* direction. Image taken from [1].

The third sample consisted of a (304) steel bent beam with a cross section of 15.7 (*x*-direction) × 18.0 (*y*-direction) mm^2. Stainless steel 304 has an austenitic FCC structure. The beam sample was subjected to four-point bending in order to induce permanent plastic deformation and a corresponding residual stress state. For the bent beam sample, the average value of elastic strain across the beam cross section was used to deduce approximately the reference unstrained lattice parameter: according to the requirement of stress balance, the net sum of compression and tension stress components is zero[1].

[1] In the beam bending approximation, stress along the beam is assumed to be simply proportional to the longitudinal strain, with the coefficient equal to the material's Young's modulus.

For all samples, it is important to consider ‘edge-effects’ due to surface stresses that can be induced during sample preparation, as this will cause deviations from the theoretical values. In the case of the aluminium ring-and-plug and quenched cylinder samples, the residual surface stress has been measured by neutron diffraction and found to be negligible compared to the magnitude of the bulk strains. Similarly, XRD measurements of surface stresses in bent beam samples prepared under similar conditions have shown these effects to be small. The presence of surface effects will act to reduce the quality of fit between theory and experiment, as models commonly do not account for stresses induced by sample processing. In all cases the match between theory and experiment (shown in section 3.3) indicate that residual surface stresses induced during sample machining can be neglected in comparison to the bulk stresses.

To validate the strain tomography reconstructions, the strain components were also mapped using energy-resolved neutron diffraction techniques. The diffraction measurements were made using the time-of-flight (TOF) spectrometer ENGIN-X at the ISIS pulsed neutron source (UK) by Dr Zhang, Dr Vorster and Prof Korsunsky. The ENGIN-X data was interpreted by Rietveld refinement of the multiple peak TOF patterns. The lattice spacing determination was carried out at each position of the diffracting gauge volume within the sample, allowing the calculation of strain components in the direction defined by the scattering vector (bisector of incident and scattered beam).

For the ring-and-plug and quenched cylinder samples that possess radial symmetry, it is convenient to define the in-plane strain components in polar coordinates, with the 'radial' direction perpendicular to the sample surface and 'hoop' direction parallel to the sample surface. For simplicity, this same coordinate system is retained here for all three samples. This is the same co-ordinate system that was used in the last chapter to introduce the theory underlying the three different strain tomography approaches.

3.3 Results for ring and plug sample

3.3.1 Ring-and-plug: Linear Tent Function Representation

The VAMAS round robin aluminium “ring-and-plug” sample has a simple and well-understood strain distribution. In principle, only minor plastic deformation is expected within the sample

and strain compatibility between the radial and hoop components should be satisfied. On this basis analytical formulae for the in-plane strains can be constructed from the elastic modulus (E) and Poisson's ratio (υ) using linear elastic solutions of the Lamé problem [14]. These equations represent full solution of the elasticity problem, and hence satisfy strain compatibility requirements:



(3.1)



(3.2)



(3.3)

Here a is the inner radius of the ring, b is the outer radius and $K=b/a$. The axial stress in the plug σ_z^{plug} and the balancing axial stress in the ring σ_z^{ring} have been measured as -15 MPa and 5 MPa respectively. The interface pressure p was determined to be 48 MPa [6]. Using Eqs. (3.1-3.3), these values give analytical expressions for the strain for comparison with the values reconstructed from neutron strain tomography. It should be noted, however, that the tomography reconstructions were performed without relying on any of the above information as *a priori* knowledge.

Fig. 3.3 shows an example of the strain compatible basis functions being used to represent the radial and hoop strain distributions. Note that the derivative of a linear interpolation (via tent functions) is a staircase due to their linearity, which we wish to preserve in order to minimise the number of unknown variables. The differential tent functions are found to provide an excellent approximation to the theoretical radial strain for the ring and plug.

Because of the discontinuity in the strain components across the boundary between the ring and plug, the solution is constructed in two parts. Figure 3.3 also illustrates that using the strain compatible tent functions to match the hoop strain implicitly also gives the corresponding radial strain. In other words applying the principles of strain compatibility, both strain components have been determined from our knowledge of just one of them via our particular choice of basis function. In spite of the limited number of data points the differential tent functions provide an excellent approximation to the theoretical radial strain for the ring and plug.

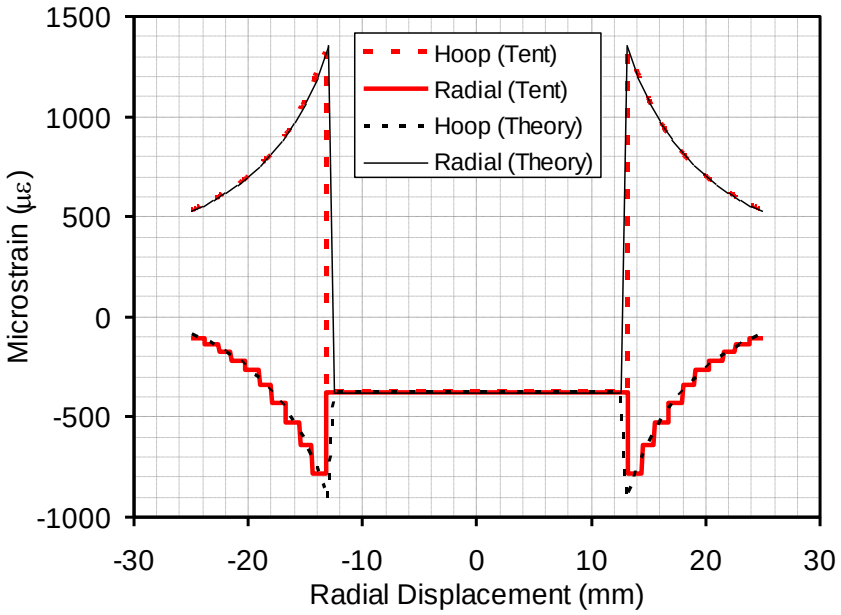


Figure 3.3: Theoretical representation of hoop and radial strain distributions and the corresponding fits using (differential) tent functions. The fits were constructed assuming knowledge of *only* the hoop component.

A comparison of the theoretical radial and hoop components derived from Eqs. (3.1-3.3) to the experimental radial and hoop components obtained from diffraction measurements [2] and strain tomography is shown in Fig 3.4. The results show a good match between the theoretical, diffraction and strain tomography data. However, because of the relatively low resolution of the strain tomography data (2 mm detector pixel size), the reconstruction fails to capture completely the behaviour of the radial and hoop strains at the ring/plug boundary.

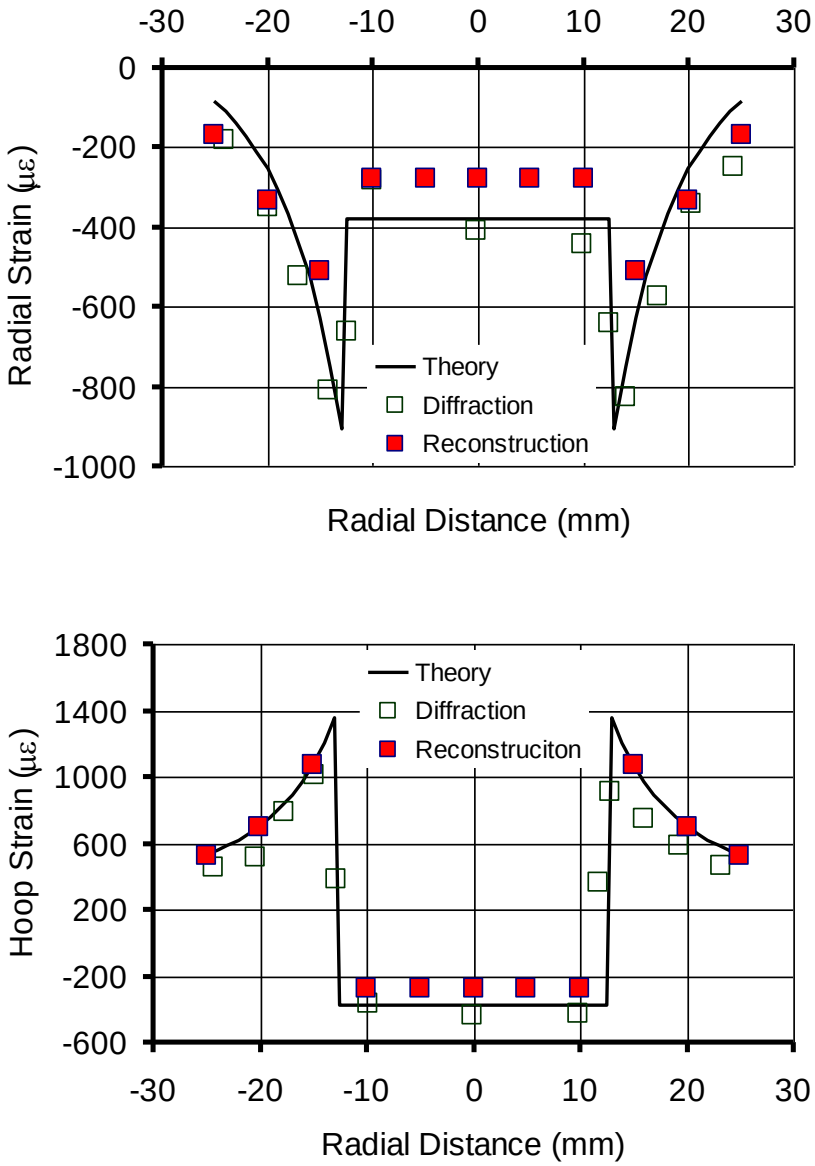


Figure 3.4: Theoretical representation of radial (top) and hoop (bottom) strain distributions and the corresponding fits using tent functions.

The corresponding fit to the experimental data used for the strain tomography reconstruction is shown in Fig. 3.5.

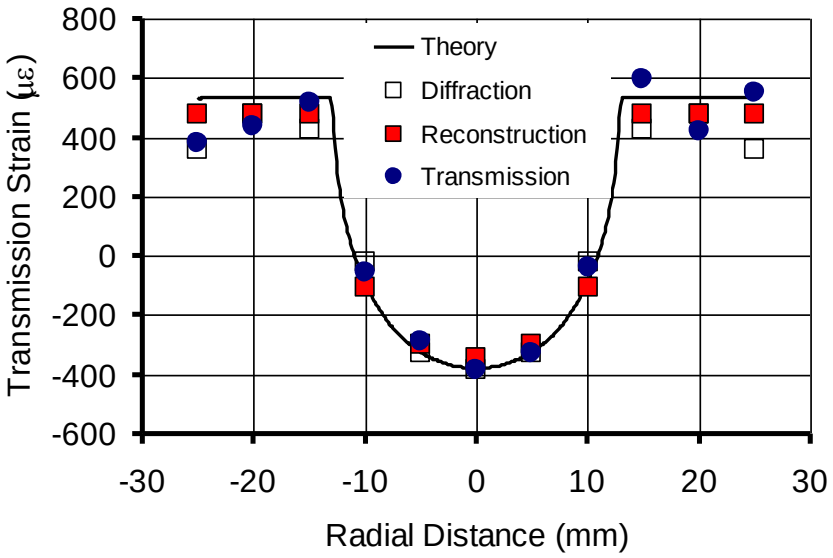


Figure 3.5: Comparison of forward calculation for theoretical, diffraction, reconstructed and transmission data.

Fig. 3.6 gives the spatially resolved strain components in the transmission direction. The four-fold symmetry in the distributions necessitates the formulation of the strain tomography problem for axisymmetric distributions in terms of a single strain component. Restructuring the problem, in terms of strain compatible basis functions ensures that the solution of the strains gives the best fit (in the least squares sense) whilst satisfying compatibility.

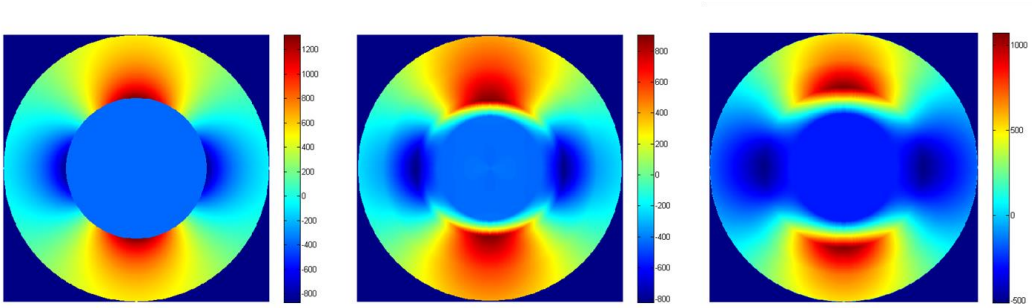


Figure 3.6: Spatially resolved transmission strain component for the theoretically predicted (left), diffraction (middle) and reconstructed strain distributions.

3.4 RESULTS for QUENCHED CYLINDER

3.4.1 Quenched cylinder: Model constraint

In order to compare the neutron diffraction data to the transmission data for the quenched cylinder, a forward calculation was performed assuming the neutron strain tomography model given by Eqns. (2.11-2.13) (see chapter 2). The hoop and radial strain profiles from the diffraction measurements were first described using the exponential-series equation (2.11). The coefficients from these equations give the column vector **c** directly. Calculating **Ac** and multiplying the result by the transpose of the average strain coefficient matrix $\overline{\varepsilon_{ij}}$ yields the prediction for the strains that would be measured at the transmission detector from a sample that has the radial and hoop strain profiles found by diffraction. The results of comparing the forward calculation of the diffraction data to the measured average strain derived from the transmission data is shown in Fig. 3.7(a). The two sets of data are in excellent agreement, providing certain degree of confidence in both the current model and the two independent experiments used to characterise the sample. Next, in order to reconstruct the radial and hoop strain profiles from the neutron transmission measurements, data shown in Fig. 3.7(a) was used to form the right hand side column vector **b** in (2.13). The coefficient vector was then determined using least-squares fitting as described above, and the results used to generate the reconstructed radial and hoop strain profiles [6].

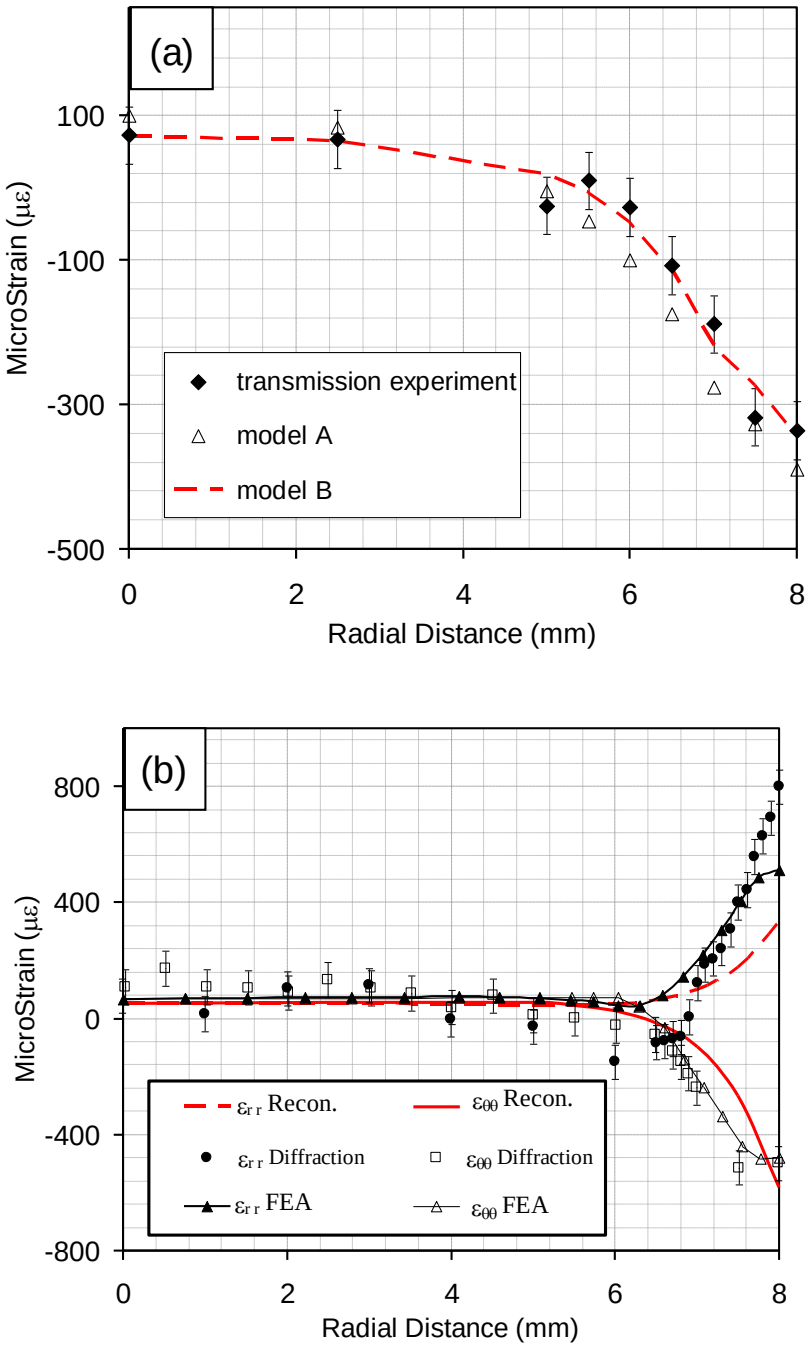


Figure 3.7. (a) Comparison of neutron transmission data to Model A: forward calculation from neutron diffraction data; and Model B: reconstruction of internal strain distributions (shown in b) by inversion of transmission data and then using forward calculation on the reconstruction. (b) The variation of hoop and radial strain components as a function of the radial distance. Strains measured by diffraction are shown by markers (filled circles and hollow squares); finite element modelling results are indicated by triangles. Reconstructed radial and hoop strain distributions are shown by the dashed and continuous lines.

Fig. 3.7(b) compares the radial and hoop strains reconstructed by inverse analysis to those measured directly using neutron diffraction. Also shown are the results of finite element analysis (FEA) to determine the strain profiles for this sample. Reconstructed profiles show reasonable agreement with the measured strain components, accurately predicting that the plastic zone extends approximately 20% into the sample [3]. It is worth noting that at the very edge of the sample the width of the gauge volume is 1mm (this is less than the pixel size of 2mm) thus, 1mm constitutes the best resolution for the transmission data. We note also that the exponential-series equation (2.11) does not describe well the variation at larger radii. These considerations account for the fact that the inverse solution is unable to resolve in sufficient detail the variation of the radial and hoop distributions at the edge of the sample.

3.4.2 Quenched Cylinder: Combined Diffraction and Strain Tomography

For the quenched cylinder sample, instead of assuming a model form for the strains, both the radial and hoop components were independently represented via the tent functions given by equation (2.5, chapter 2) without assuming compatibility. To reconstruct the strains, prior knowledge of the radial strain at the edge of the sample and the hoop (and radial) strain in the centre of the sample was assumed. This information came from independent diffraction measurements of the strain components in these locations. During the reconstruction the radial strain at the edge and hoop strain in the centre were constrained to be within 10% of the measured diffraction strain. Weighting toward a 'smooth' solution was still enforced according to Eq.(6). The result of including the two diffraction points in the calculation of the strain components is shown in Fig. 3.8.

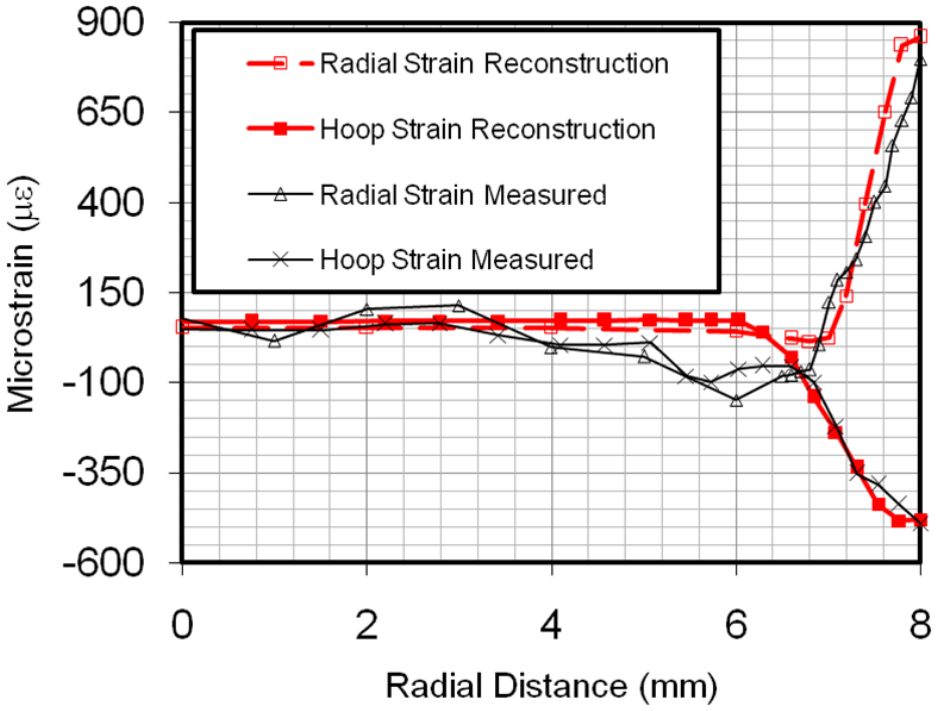


Figure 3.8. (a) Comparison of neutron diffraction data for the radial and hoop strains for the quenched cylinder to the strain profiles obtained using a linear tent function representation of the strains. Two values for the strain profiles were assumed to be known in the tent function representation: the data point at the edge of the sample for the radial strain and the data point in the centre of the sample for the hoop strain.

3.5 Results for Steel Bent Beam

3.5.1 Steel Bent Beam: Comparison with Finite Element Modelling

The first demonstrations of strain tomography described in Chapter 2 as well as the VAMAS ring-and-plug results described in this chapter assumed a functional fit to the unknown strain distributions based on *a priori* information - normally obtained from finite element (FE) modelling. Extending this idea of a model approach therefore, the next logical step is to use a general modelling package, e.g. based on finite elements, and to attempt to adjust the process parameters to match the experimental data. The ring-and-plug and quenched cylinder samples possessed a radially symmetric strain distribution and therefore only necessitated a Bragg-edge

transmission measurement at a single sample orientation to capture the strain profile. For the steel bent beam the strain distribution is not symmetric and therefore multiple projections of the average strain are required to model the complete profile.

The data upon which the analysis of the bent beam strain profile is based are plots of the average transmission strain as a function of angular rotation. We term this data a 'strainogram' in reference to the sinograms used to represent the raw information in standard computer tomography. Since the relative contribution of the in-plane strain components are a spatially varying function of angle, they cannot be directly related to the strainogram in the same way that multiple projections of the sample density may be related to a sinogram. This is illustrated in Fig. 3.9 where the contribution to the measured transmission strain is shown for a number of different sample rotations for simulated bent beam data.

In order to obtain an estimate for the in-plane strains, a finite element simulation of the bent beam was carried out and a forward calculation used to match the simulated data to the experimental measurement. This approach, whilst not a direct reconstruction from the experimental data, allows a confirmation of the sample process conditions and can be used to distinguish between competing FE models for more complex samples.

To perform the comparison of simulated to experimental data, the radial and hoop strains from the FE model are entered into Eq 2.7 and the sample rotation chosen to match the actual experiment. As with the previous sample, the result is then summed along the transmission direction and normalised by the sample thickness to give the average strain as a function of the sample rotation. The sample thickness for each rotation angle is obtained by setting all the pixels within the object to one and calculating the corresponding sinogram.

A comparison of the strainogram obtained from experiment with the one from the forward simulation of the finite element model is shown in Fig. 3.10; a plot comparing the simulated and experimental data for the 90 degree sample rotation angle is shown in Fig. 3.11.

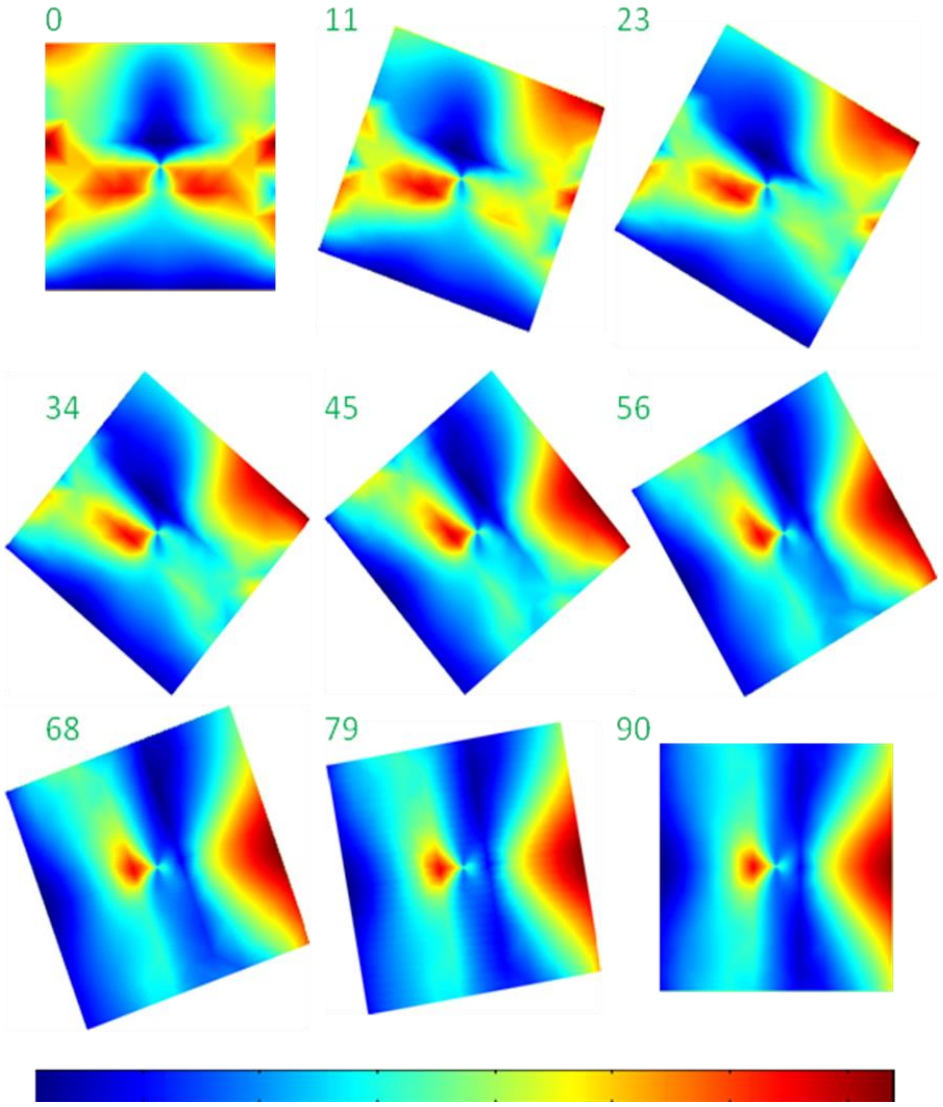


Figure 3.9: The simulated transmission strain component for a bent-beam cross-section for nine different sample rotation angles.

The differences between the experimental and simulated results may in part be attributed to the fact that the sample geometry assumed for the two approaches was different; in the simulation the cross section was taken to be square, whilst in the experiment it was rectangular. The reason for the difference in the shape of the simulated and experimental samples is because of the fact that further machining of the steel bar could induce additional residual surface stress. As the simulations were carried out prior to the exact dimensions of the experimental sample dimensions being known accurately, there is a small discrepancy between the two. Another major factor in deviation between experiment and theory is the finite resolution of the detector

($2 \times 2mm^2$) which limits the number of experimental data points across the smallest dimension of the sample to just six. The bending force and other process parameters in the simulation were chosen to match the experiment.

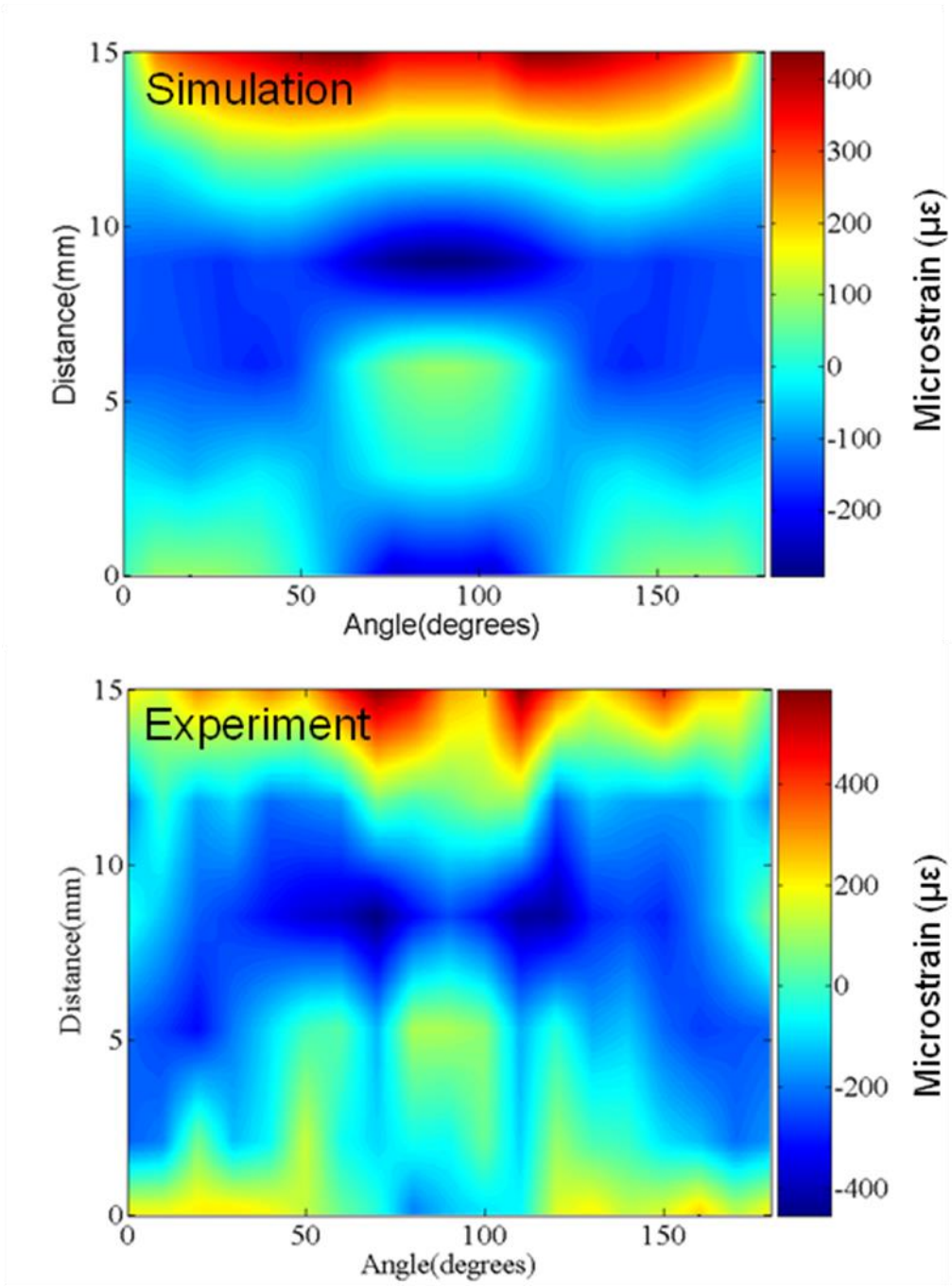


Figure 3.10: Comparison of the strainogram, which displays the average sample strain in the transmission direction as a function of the sample rotation, obtained from the strain tomography experiment with the one obtained from the forward simulation of the finite element model.

Work is currently underway to incorporate a reconstruction of the strain components directly into the commercial FE framework. When combined with volume rendered data from absorption tomography this would enable reconstruction of the strains without using any a priori information about the sample. For the present data, the main factor preventing a direct reconstruction of the strains, similar to the approach used for the aluminium sample, is the coarse resolution of the detector in comparison to the variation of the strain field being reconstructed. In the future, we anticipate that the significantly higher resolution offered by micro-channel plate (MCP) neutron detectors will enable the direct reconstruction of non-axisymmetric stain fields. Nonetheless, the results reported here represent the first time that the non-axisymmetric neutron strain tomography problem has been addressed.

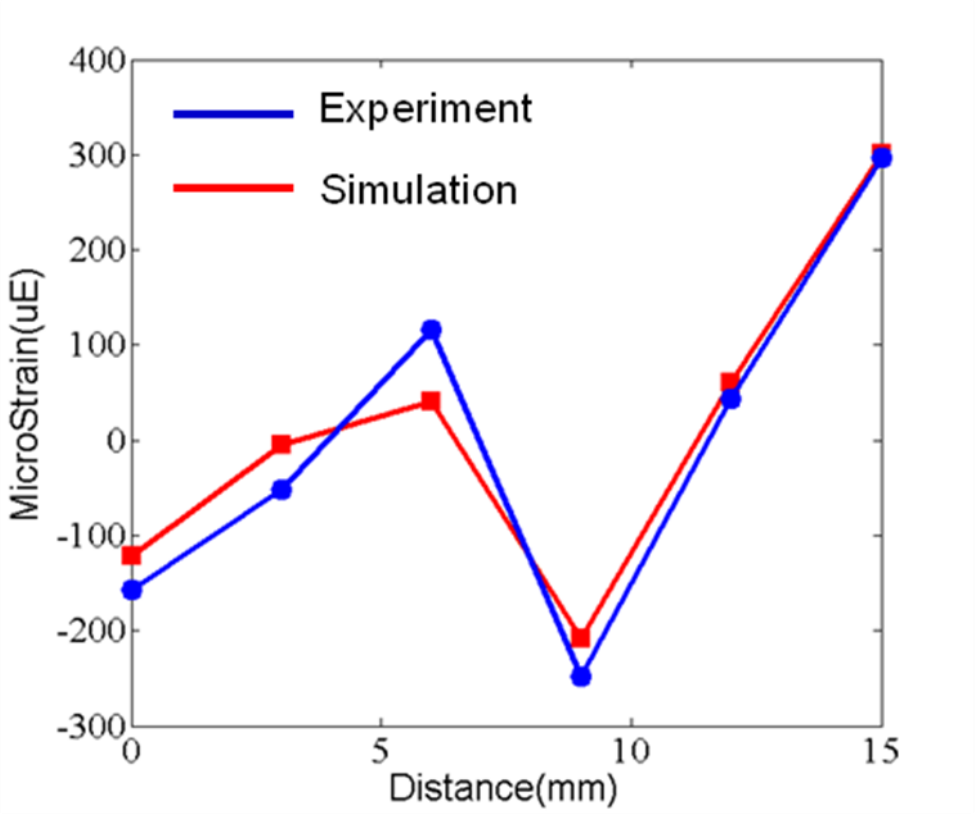


Figure 3.11: Plot comparing the value for the average strain from simulation to experiment at 90 degrees sample rotation.

3.6 SUMMARY of APPROACHES

In this chapter the principle of neutron strain transmission tomography has been demonstrated for three samples. Two of these, the VAMAS "ring and plug" and the quenched cylinder samples possessed an axially symmetric strain distribution, whilst the third, a bent beam, was non-axisymmetric. For the "ring and plug" sample, the reconstructed strain distributions are represented using differential tent functions in which strain compatibility is enforced implicitly in the solution. The strain compatible basis function method outlined in this chapter allows the strain tomography problem to be reformulated in terms of a single strain component when only the in-plane strains need to be considered. The problem is thus analogous to conventional absorption tomography and, provided the strain distribution is sufficiently well sampled, yields a unique solution for the strain components.

The second sample, the quenched cylinder, was reconstructed using both a constrained model approach assuming prior knowledge about the functional form of the distribution. In this case the strain distribution was known to closely follow an exponential-power series representation (Eq 2.5), which was confirmed though FE modelling. This regularises the problem, reduces the number of parameters to be found by fitting, and leads to a stable solution. The approach can only be used for a limited range of problems. In terms of extending the method to arbitrary non-axisymmetric distributions therefore, it remains to be researched further to see how the functional model approach should be applied for best results.

The approach used to analyse the strains for the third sample was to compare the results of neutron strain tomography with finite element simulations. The general form of the strainograms obtained from the experiment and simulation were found to be similar. Deviations of the experimental data from the simulation prediction can be explained in terms of differences in the sample geometry assumed between the two methods. Future work will concentrate on implementing neutron strain tomography within the framework of a standard commercial FE package. This approach would certainly regularise the problem, reduce the number of parameters to be found by fitting, and should lead to a robust method for retrieving the strains.

The limited flux available at neutron sources has long been regarded as one of the fundamental limitations on using the technique for strain characterisation of engineering components. For

the examples presented in this chapter the data collection time for the diffraction data was ~ 2 minutes/point (i.e. 20 minutes to cover the entire sample) compared to 2.5 minutes required to build up sufficient statistics to measure Bragg edges. We therefore estimate that strain tomography would offer an improvement factor of around 8 for the total time taken to collect the data -neglecting the time for motor moves etc. required for neutron diffraction.

The work presented in this chapter represents an important step towards the implementation of strain tomography for the reconstruction of arbitrary three dimensional strain distributions. In addition, the recent development of micro-channel plate (MCP) detectors offers the possibility of improving the resolution of the method to the 0.01 mm scale, though there obviously would be a concomitant increase in the time for data collection. Such high-resolution imaging is currently not a practical possibility for neutron diffraction due to the physical limit on the degree of collimation. However, binning the data after collection allows selecting the effective spatial resolution from a range of values between 0.01mm and 1mm.

3.7 REFERENCES

1. Abbey, B, S. Y. Zhang, W. J. J. Vorster and A. M. Korsunsky, *Reconstruction of axisymmetric strain distributions via neutron strain tomography.* NIM. Section B: Beam Interactions with Materials and Atoms. 2012. 270:28-35.

2. Daymond, M.R., M.W. Johnson, and D.S. Silvia, *Analysis of neutron diffraction strain measurement data from a round robin sample* The Journal of Strain Analysis for Engineering Design, 2002. **37**(1): p. 73-85.

3. Vorster, W.J.J., *DPhil Thesis*, in *Engineering Science*. 2007, Oxford.

4. Johnson, M.W., L. Edwards, and P.J. Withers, *ENGIN -- A new instrument for engineers.* Physica B: Condensed Matter, 1997. **234-236**: p. 1141-1143.

5. Zhang, S.H., *DPhil Thesis*, in *Engineeing Science*. 2008, Oxford.

6. Abbey, B, S. Y. Zhang, W. J. J. Vorster and A. M. Korsunsky, *Feasibility study of neutron strain tomography.* Procedia Engineering, 2009. **1**(1): p. 185-188.

CONCLUSIONS AND SUGGESTIONS FOR FUTURE WORK

CHAPTER 4

4.1 INTRODUCTION

This thesis has summarised progress in the field of neutron strain tomography, an approach that builds upon the physics of neutron diffraction and the formation of Bragg edges that are the basis for neutron transmission strain measurements. The approaches to the inverse problem of reconstructing the unknown strain components from measurements of the average transmitted strain have been outlined. Experimental results that have been obtained for radially symmetric strain distributions have been summarised, together with the first attempt to retrieve information from non-axially symmetric data. In this final chapter an assessment of the different approaches to neutron strain tomography is given, the current feasibility of the technique is discussed and the possibilities for future work are described, particularly in the context of emerging detector technologies.

4.2 COMPARISON OF APPROACHES TO NEUTRON STRAIN TOMOGRAPHY

In chapter two, the fundamentals of the strain tomography problem were introduced and a summary of approaches, prior to the work described in this thesis, was given. Three different solutions to the problem of reconstructing spatially resolved strain distributions were discussed: the representation of the unknown strains through linear tent functions, the use of simple analytic functions to describe the strain variation, and a combination neutron strain tomography with limited data from conventional neutron diffraction.

The representation of the unknown strain distributions via linear tent functions provides the most general approach to strain tomography, as no *a priori* information is assumed. The representation of

the unknown strain profile by the overlapping set of tent functions leads to regularisation of the solution for unknown strains; yet, in combination, the basis set of tent functions possesses a large degree of flexibility and can be used to represent a wide range of arbitrary strain distributions. However, the tent function basis cannot address fully the 'ill-posedness' of the strain tomography problem. Namely, we note that there exist two degrees of freedom per sample voxel (ignoring the out-of-plane strain components), so that there are a greater number of unknowns than the number of measured data points. In addition, at some points on the detector the measured strain contains contributions from only one component, so that all information about the other component is lost for that location. In principle, it can be shown that these problems can be addressed by enforcing strain compatibility that provides a fundamental link between the strain components. In practice though, it was found that strain compatibility only works well when the data quality is extremely good, since very small variations in the gradient of one strain component may produce very large changes in the value of the other component through the application of the compatibility equation (e.g. in the axially symmetric case). If the strain component that is varying steeply does not contribute significantly to the average strain, then large strain variations may have little influence on the quality of fit to the measured data, ultimately leading to an inaccurate result. This is illustrated by the fact that strain compatible tent functions produced a satisfactory result for the strain profile of the VAMAS ring-and-plug sample but were unsuccessful at determining the radial and hoop strain distributions for the quenched cylinder [1]. To summarise, although tent functions represent a simple and effective means of representing the spatially resolved strain fields, for the problem of tomographic strain reconstruction, without additional information about the problem they may not form a reliable means of mapping the residual elastic strain profile.

The simplest means of obtaining a reasonable reconstruction of the unknown strain distribution is to use an analytic model for the shape of the distribution prior to reconstruction. For example, in an earlier demonstration of strain tomography by Zhang et al. on a ring-and-plug sample, the functional forms for the strain distributions (eqns 3.1 to 3.3 in chapter 3) were assumed [2]. A least squares fit to the data was then used to determine the value of the parameters describing these distributions. Because of the heavily constrained nature of the problem, the general form of the distributions is thus fixed to be correct. Also, since the number of parameters to fit is generally small, the problem is heavily over-determined in this case. A similar “over-constraint” idea was behind the choice of exponential functions to represent the ring and hoop distributions from the quenched cylinder shown in chapter 3. The results show that the general form of the distributions is well-represented by the exponentials, but that the fine details of the distributions is lost, e.g

where they vary rapidly at the edges [3]. This highlights both the strength and weakness of the constrained model approach, since it illustrates that a reasonable answer can only be obtained provided the measured distributions satisfy the model constraints imposed on them. The biggest drawback of a model approach is, of course, that this method of determining the unknown strain distributions requires detailed knowledge about the general form of the strain distributions in the sample before reconstruction of the strains can begin.

The third and final method tried for the reconstruction of the unknown strain distributions was to use combined neutron strain tomography and neutron diffraction. In this approach, the unknown strains are represented via tent functions but the problem is regularised through the inclusion in the inversion process of a few known strain data points for measured by neutron diffraction. There are several issues with this approach. The first is that due to the spatially varying contributions of the unknown strains to the average transmitted strain profiles, the measurement of one strain component alone is not sufficient. The selection of the strain component to be measured depends on the position of that component within the sample. This choice therefore requires some prior knowledge of the sample geometry. In spite of the need to characterise the shape of the sample beforehand, a combination of neutron strain tomography and diffraction is currently the most reliable means of extracting arbitrary unknown strain profiles. The exact number of diffraction points required in the inversion process is difficult to quantify due to the number of factors involved that include the measurement resolution, the shape of the sample, the complexity of the strain distribution, and how quickly it varies. For the two samples that we examined using this method, the inclusion of just two known diffraction points- one for the hoop and one for the radial distribution – yielded excellent results.

4.3 FUTURE WORK

4.3.1 Literature Review: High-resolution Neutron Strain Imaging

One of the most exciting developments in neutron strain imaging is the availability of high-resolution energy dispersive (Time-of-Flight) detectors. The ability to correlate high-resolution transmission absorption data with spectrally resolved information opens up a number of new possibilities for research. In particular it has major implications for the field of neutron strain tomography, where the spatial resolution of the measurement (currently 2.5 mm) is a serious limitation on the amount and quality of data available for reconstruction.

One of the earliest reports in the literature on the use of high-resolution energy resolving neutron detectors was by Tremsin et al. in 2008 [4]. In this work, a neutron-sensitive micro-channel plate detector (MCP) utilising a Medipix2 electronic readout was tested at the ISIS neutron source. The detector contained 256 × 256 square pixels of just 55 μm length. The converter layer to allow the detection of neutrons contains either ^{6}Li or ^{10}B which convert the neutrons into heavy charged particles recoiled from a polyethylene film. The energy resolution of the detector corresponded to ΔE/E ~0.1%, sufficient to resolve Bragg edges. Two samples were studied, an iron cylinder filled with a copper rod (Fig 4.1) and a rolled aluminium plate (not discussed here).

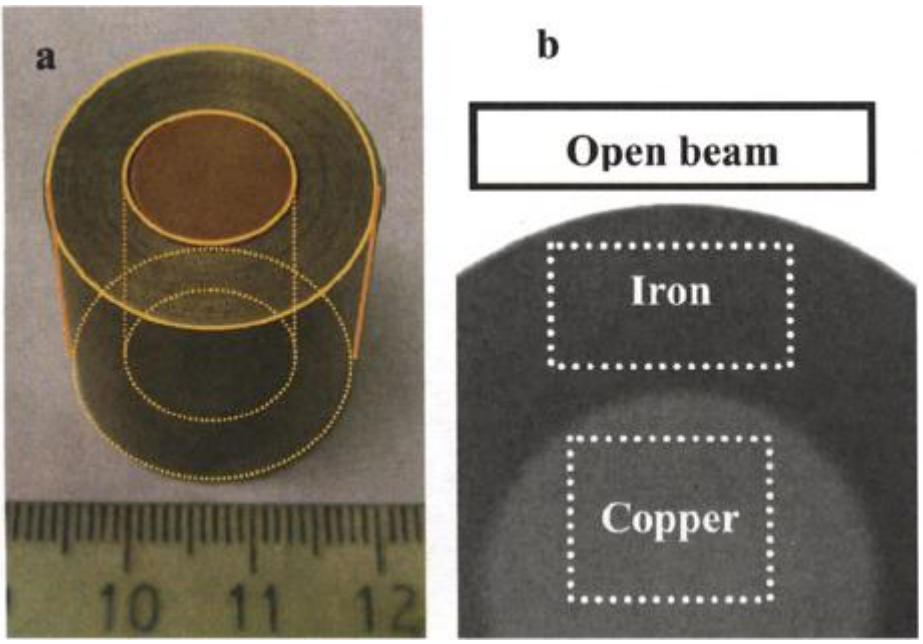


Fig. 4.1. (a) Photo of the Iron/Copper cylinder sample (25 mm outer diameter) with a press fit copper rod interior (10 mm outer diameter). The cylinder height was 25 mm and it was placed end-on in the beam for these measurements. The full-transmission image at 55 μm resolution - the result of integrating counts over the entire spectrum for 6 minutes is shown in (b). Taken from [4].

A typical transmission image, the result of integrating counts over the entire spectrum is shown for the Iron/Copper cylinder (placed end on) in Fig 4.1b. The resolution of this measurement is determined by the smallest pixel size 55 μm. The white dotted boxed regions in Fig 4.1b show the areas of the sample over which the counts were integrated in order to produce the Bragg-edge data given in Fig 4.2. The total integration time to produce the energy-resolved spectra within each of these regions was 20 seconds, with TOF resolution of 100 μs used. This is due to the fact that the statistics on the spectra obtained with full pixel resolution was insufficient to determine the position of the Bragg edges.

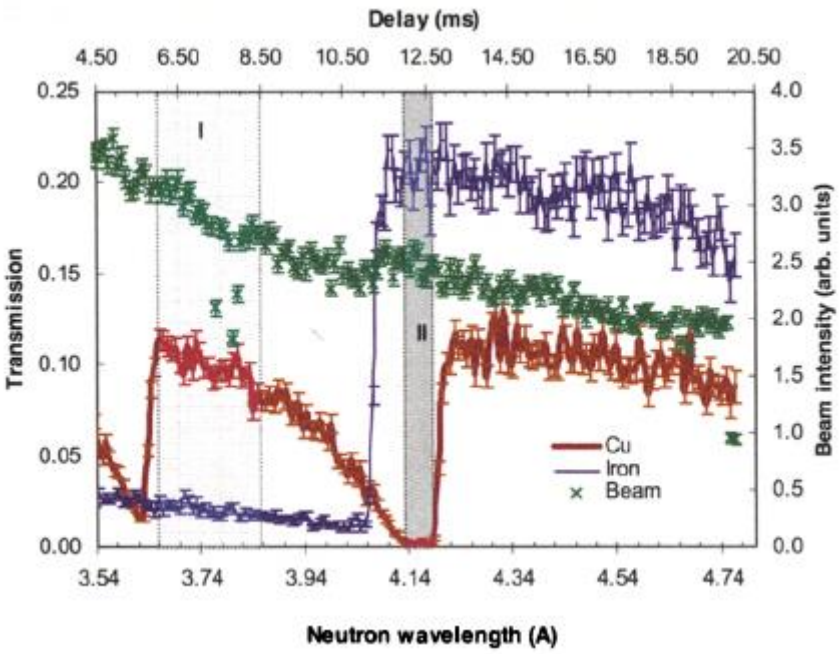


Fig 4.2. The energy-resolved transmission spectra measured for the Iron and Copper cylinders corresponding to the sample area enclosed by the white dotted boxes in Fig. 4.1. The resolution of the measurements is 100 μs and the integration time is 20 seconds.

By summing data within the range 3.66-3.86 Å and within 4.14-4.18 Å, two images were obtained; one where the transmission of the iron was less than the copper (before the iron edge) and one where the transmission of the iron is greater than the copper (after the absorption edge). A comparison of these two images is shown in Fig. 4.3. The difference in contrast depending of the placement of the integration range above or below the iron edge is striking.

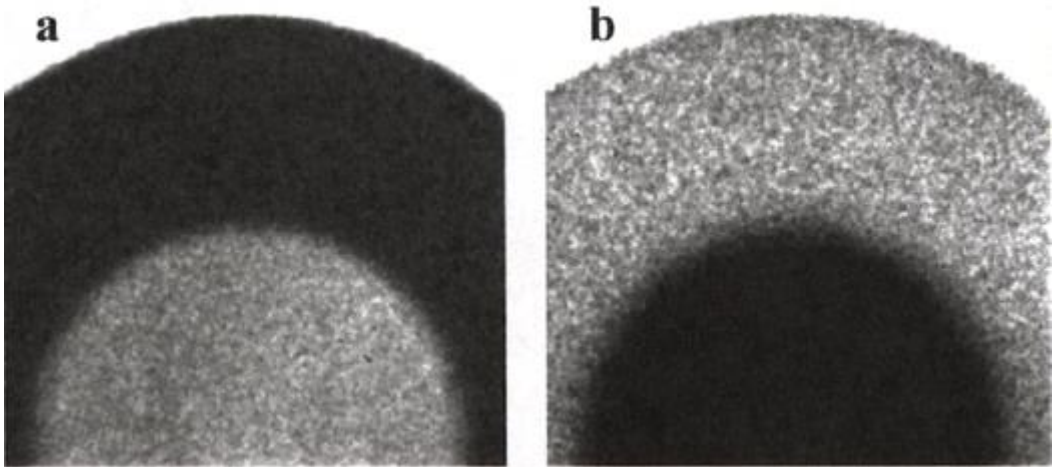


Fig 4.2. Transmission images of the iron/copper cylinder sample taken at (a) 3.66-3.86 Å, where iron is more opaque than copper (before iron edge) and (b) at 4.14-4.18 Å, where copper is more opaque than iron (after iron edge).

One limitation noted was that at full resolution, the time to collect sufficient statistics to record a Bragg edge can become prohibitive. A suggested solution to this is that the absorption information for the sample (that can be collected using the full spectrum) can be obtained at full resolution. The Bragg-edge data necessary for strain analysis can then be extracted by binning data down to a lower resolution, i.e. combining data from neighbouring pixels or integrating over entire areas, as was done in [4].

The limits on the resolution for neutron detection achievable with MCP technology were discussed in [5]. The authors demonstrate that neutron detection with a positional accuracy of better than 15 μm is possible due to the fact that the mean free path of the secondary products of neutron interaction with the MCP is just a few microns. Thus, the electron avalanche associated with each individual neutron detection event is limited to just 1-2 channels of the detector - normally 6 - 10 μm across. To confirm the spatial resolution of the detector transmission, images of a Gd pinhole mask and a cluster of 20 - 50 μm B_4C particles suspended in epoxy were taken. Cross-sections through the transmission images were measured, demonstrating FWHM corresponding to the resolution better than 15 μm. The limit of spatial resolution of the TimePix detector for ultra cold neutrons (UCN) was explored in [6]. The conversion efficiency for cold neutron sources (~40%) is around twice that for thermal sources (~20%). Using a ^{6}LiF conversion layer for detection, the authors were able to demonstrate a sub-pixel resolution of just 1 μm. These results were confirmed through Monte Carlo simulations of the point spread function for the detector. Although per-pixel detection rates for these high-resolution detection set ups is comparatively low [4], these findings indicate that, in the future, it may be possible to determine strain with micron precision.

One of the first published demonstrations of the use of the Timepix detector for strain determination was reported in [7] at the SNAP beamline of the ORNL spallation neutron source. In this work, a two-dimensional map of Bragg edge positions for the Fe 110 reflection were recorded for a bent steel screw sample (Fig. 4.3). From the positions of the Bragg edges values for the average transmission strain were determined with an accuracy of a few hundred microstrain (ppm) based on a total data collection time of 300 s. The resolution for the strain measurement was determined by the pixel size of the detector which was 55 μm. An example fit to the Fe 110 Bragg edge corresponding to a single detector pixel and the resulting two-dimensional strain map for the steel screw sample are shown in Fig. 4.4. These measurements demonstrate the suitability of the TimePix detector for development of high-resolution neutron strain tomography.

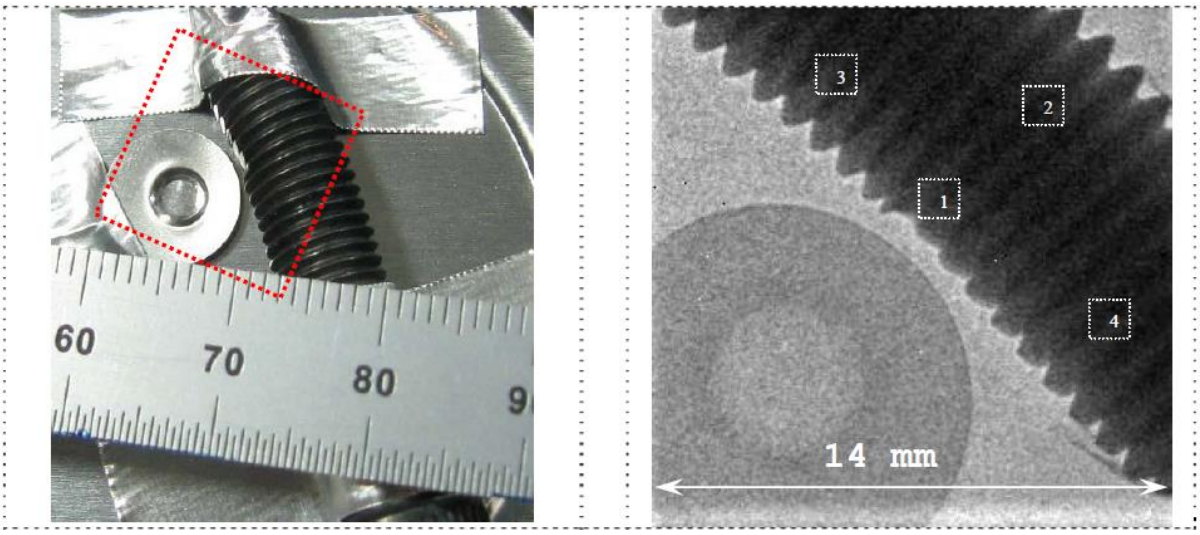


Figure 4.3. Left: Photograph of a bent steel screw that was used for the transmission strain measurements with the TimePix detector. The dashed square shows the 14 x 14 mm^2 area that was illuminated by the neutron beam. Right: Neutron transmission image of the area contained within the dashed square using the full incident spectrum.

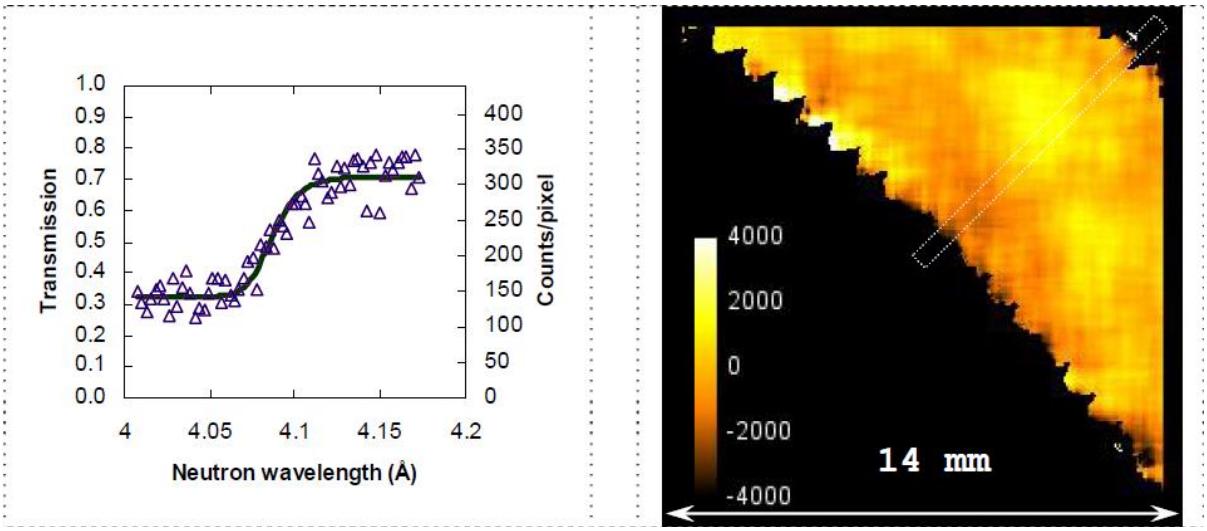


Figure 4.4. Left: Example measured Bragg edge for the Fe 110 reflection. An analytical fit to the edge which was used to determine the Bragg edge position to within a few mÅ is shown by the solid black line. Right: The result of measuring the Bragg edge position across a portion of the screw shown in Fig. 4.3. The scale bar shows the average transmission strain in με (microstrain).

Strain measurements using the TimePix detector have also been published based on the data collected on the ENGIN-X beamline at the ISIS pulsed spallation source. Strain data were collected from the VAMAS round robin shrink fitted aluminium ring-and plug (described in

chapter 3) with a resolution better than 200 με. As in [7], the resolution of the measurement was determined by the pixel size - 55 με. The average strain profile determined using the TimePix detector agrees well with the theoretical strain profiles for the round robin sample (also presented in chapter 3).

More developments on the detector processing electronics are required in order to reduce the data acquisition times by enabling simultaneous measurements of spectra in a wide energy range covering multiple Bragg edges. In order to reduce the data collection times, the strain data for ring-and-plug cylinder were summed in the y-direction (Fig. 4.5). The result of fitting the Bragg edge positions in order to determine the average transmission strain in the x-direction in shown in Fig 4.5.

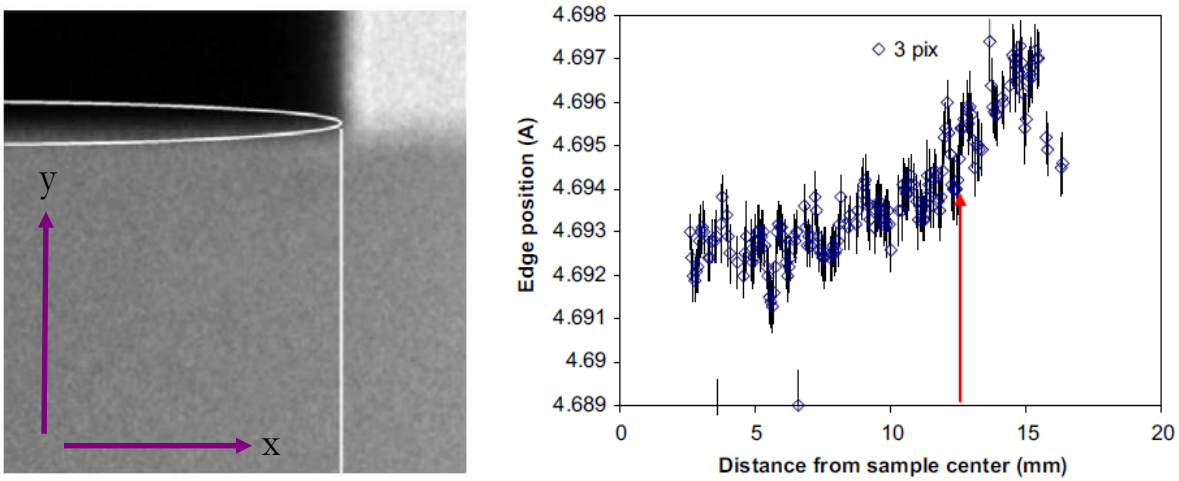


Fig. 4.5. Left: Neutron transmission image from the VAMAS aluminium ring-and-plug sample. An iron bar was placed on top of the sample - dark rectangle at the top of the image, for alignment. The white outline indicates the position of the inner cylinder. Right: Strain determined from fitting the Bragg edge positions for pixels in the x-direction. This profile shows some similarities with the theoretical average strain profile for this sample (chapter 3). However, the published data only show a small portion of the sample, less than half the diameter, and therefore cannot be used for strain tomography.

These results from the TimePix detector present a clear path to overcoming one of the key issues with previous strain tomography experiments - namely the insufficient resolution of the measurement. One issue that still remains, however, is balancing the resolution of the measurement against the time required to collect the data. Although as yet there have not been any

opportunities to use the TimePix detector for this strain tomography project, we have been able to produce some preliminary results from the VAMAS ring-and-plug data.

4.3.2 Latest results: strain tomography using TIMEPIX

A second set of TimePix transmission data for the VAMAS ring-and-plug sample was collected in 2011. The results are shown in Fig. 4.6. Unlike Fig. 4.5, the entire half of the sample is contained in the beam. Therefore it is possible to characterise completely the axisymmetric ring-and-plug strain distribution. Based on the total transmitted intensity with the full beam, a standard absorption tomography reconstruction of the ring-and-plug sample can be carried out. This is also shown in Fig. 4.6. The absorption tomography reconstruction could be used as input to define the sample boundary for the strain tomography reconstruction.

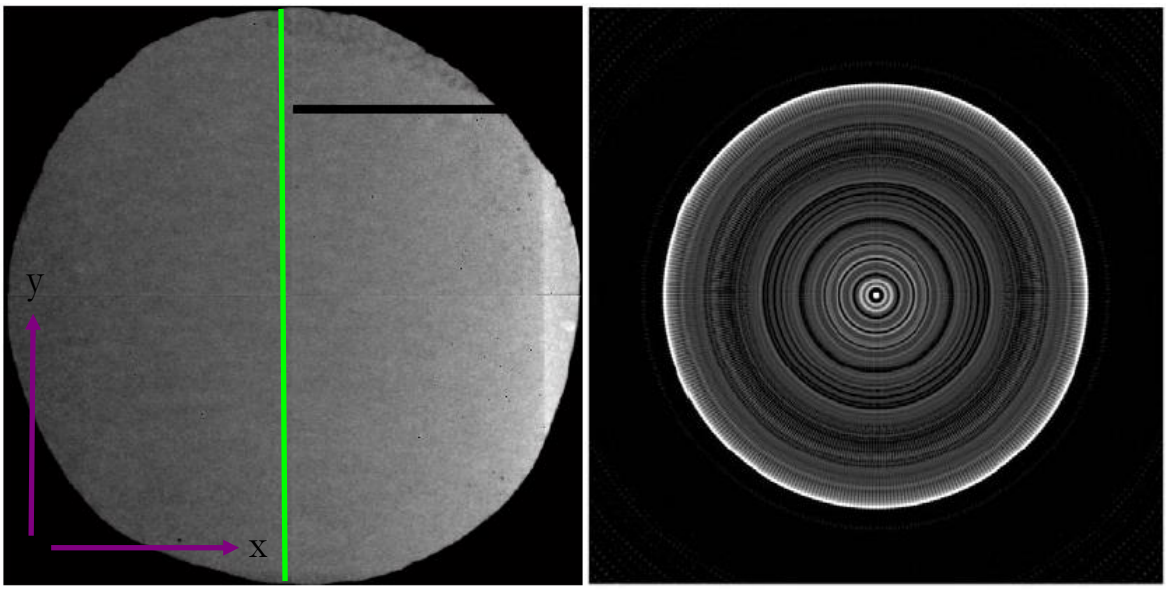


Fig. 4.6. Left: Transmission image of half of the VAMAS ring-and-plug sample, the green line defines the approximate boundary between the outer and inner rings. Right: reconstruction of absorption tomography slice from ring-and-plug sample based on the transmission full-beam data.

Summing the Bragg-edge data in the y-direction gives sufficient statistics to extract strain in the x-direction. An example Bragg-edge dataset and corresponding sigmoidal fit is shown in Fig. 4.7. The Bragg edge data as a function of the sample position in the x-direction is shown on the RHS of Fig. 4.7. The experimental data clearly show that the position of the Bragg-edge shifts as you move from the centre of the ring-and-plug sample to the surface. Also shown is the Bragg-edge data as a function of the y-position. In this case the position of the Bragg edge is constant since there is no residual strain profile in this direction - confirmation of the variation seen in the x-direction. Fitting

of all the Bragg edges in the x-direction and comparing to the unstrained value for the VAMAS sample (see chapter 3) yields the plot shown in Fig. 4.8 which represents the variation of the residual elastic strain in the x-direction from the centre of the ring-and-plug to the edge. This plot is very similar in form to the much lower resolution data shown in Fig. 3.5. Hence, it should be possible to extract the spatially resolved radial and hoop strain distributions for the VAMAS sample via strain tomography at a resolution of 55 μm. Work is currently underway to try and invert this data to obtain very-high resolution, spatially resolved strain information.

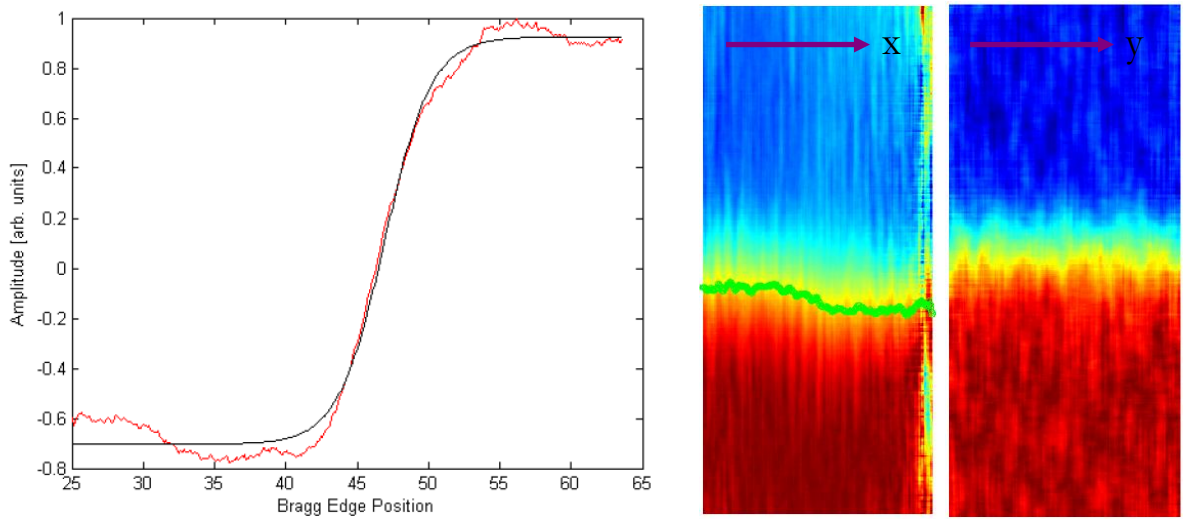


Fig. 4.7. Left: Example Bragg-edge profile (red line) and corresponding sigmoidal fit. Right: Bragg edges obtained by summing spectral data in the y-direction (i.e. variation in x-position) and by summing in the x-direction. As expected the sample shows a clear variation in the Bragg-edge position in the x-direction, but almost no variation along the y-direction. The Bragg edge data is plotted on a linear scale where blue corresponds to the amplitude of ~-0.8, and red to the amplitude of unity.

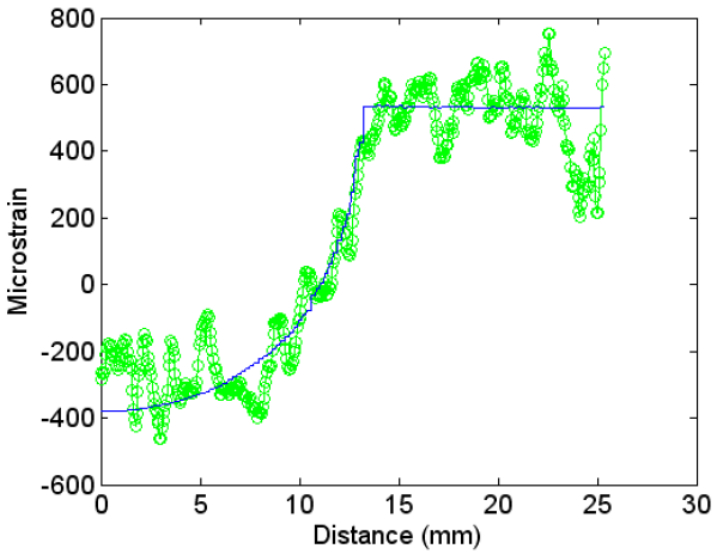


Fig. 4.8. Strain variation obtained using TimePix detector data along the x-direction of the VAMAS sample. Unlike the data published in [7], this data set covers the full sample radius and has better signal-to-noise characteristics.

4.3.3 Future research: planned experiments and ideas for further work

Our preliminary analysis of the TimePix data for the VAMAS ring-and-plug sample has given us significant confidence that the data can be used for strain tomography and will address many of the resolution issues that persist with the current detector (2 mm pixels). Further strain tomography experiments using the TimePix detector are planned for September. We aim to reconstruct in three-dimensions a non-axially symmetric strain profile from 90 projections at a resolution of 55 μm. This will be more than an order of magnitude improvement in the resolution of the strain tomography data collected thus far. It is hoped that it will form the foundation for developing the technique into an advanced characterisation tool for engineering applications.

4.4 REFERENCES

1. Abbey, B., S.H. Zhang, W.J.J. Vorster, and A.M. Korsunsky, *Reconstruction of Axisymmetric Strain Distributions via Neutron Strain Tomography* In preperation, 2011.

2. Zhang, S.Y., B. Abbey, P. Xu, Y. Tomota, and D. Liljedahl, *Materials Structure and Strain Analysis Using Time-of-flight Neutron Diffraction* WORLD CONGRESS ON ENGINEERING, 2009. **1**(1).

3. Abbey, B., S.Y. Zhang, W.J.J. Vorster, and A.M. Korsunsky, *Feasibility study of neutron strain tomography*. Procedia Engineering, 2009. **1**(1): p. 185-188.

4. Tremsin, A.S., J.B. McPhate, W.A. Kockelmann, J.V. Vallerga, O.H.W. Siegmund, and F.W. Bruce;, *Energy-Resolving Neutron Transmission Radiography at the ISIS Pulsed Spallation Source with a High-Resolution Neutron Counting Detector*.

5. A.S.;, T., V. J.V.;, M. J.B.;, S. O.H.W.;, F. W.B.;, C. L.;, and C. R.G.;, *On the possibility to image thermal and cold neutron with sub-15 micon spatial resolution*. Nuclear Instruments and Methods in Physics Research A, 2008. **592**: p. 374-384.

6. Jakubek, J., P.Schmidt-Wellenburg, P.Geltenbort, M.Platkevic, C.Plonka-Spehr, J. Solc, and T.Soldner, *A coated pixel deviceTimePix with micron spatial resolution for UCN detection*. Nuclear Instruments and Methods in Physics Research A, 2009. **600**: p. 651-656.

7. A S Tremsin, J B McPhate, J V Vallerga, O H W Siegmund, W B Feller, H Z Bilheux, J J Molaison, C A Tulk, L Crow, R G Cooper, and D. Penumadu, *Transmission Bragg edge spectroscopy measurements at ORNL Spallation Neutron Source*. Journal of Physics: Conference Series 251, 2010: p. 012069.

APPENDIX PUBLICATIONS ARISING FROM THIS WORK

1. Abbey, B., S.Y. Zhang, W.J.J. Vorster, and A.M. Korsunsky, Feasibility study of neutron strain tomography. Procedia Engineering, 2009. 1(1): p. 185-188.

2. Zhang, S., E. Godfrey, W. Kockelmann, A. Paradowska, M. Bull, A. Korsunsky, B. Abbey, P. Xu, Y. Tomota, and D. Liljedahl, High-tech composites to ancient metals. Materials Today, 2009. 12(7-8): p. 78-84.

3. Abbey, B., S.Y. Zhang, W. Vorster, and A.M. Korsunsky, Reconstruction of Axisymmetric Strain Distributions via Neutron Strain Tomography. Nuclear Instruments and Methods in Physics Research Section B: Beam Interactions with Materials and Atoms, 2011.

4. Abbey, B., S.Y. Zhang, M. Xie, X. Song, and A.M. Korsunsky, Neutron strain tomography using Bragg-edge transmission. International Journal of Materials Research, 2012. 103(2): p. 234-241.